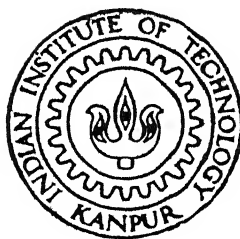# Unstable Crack Propagation In Drawn Steel Wire
A Study on Crack Tip Plastic Flow And Effect of
Warm Pre-Stressing on Fracture Toughness of Mild Steel

by

S. SRIDHAR

DEPARTMENS OF MECHANICAL ENGINEERING
INDIAN INSTITUTE OF TECHNOLOGY KANPUR
NOVEMBER 1997

UNSTABLE CRACK PROPAGATION IN DRAWN STEEL WIRE

A STUDY ON CRACK TIP PLASTIC FLOW AND EFFECT OF

WARM PRE-STRESSING ON FRACTURE TOUGHNESS OF MILD STEEL

A THESIS SUBMITTED

IN PARTIAL FULFILMENT OF THE REQUIREMENTS

FOR THE DEGREE OF

MASTER OF TECHNOLOGY

By

S. Sridhar

to the

DEPARTMENT OF MECHANICAL ENGINEERING
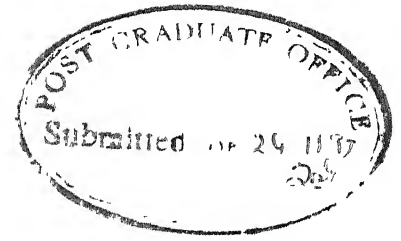
INDIAN INSTITUTE OF TECHNOLOGY

KANPUR–208016 INDIA

NOVEMBER 1997

ME- 1997 -M- SRI-UNS

CERTIFICATE

It is certified that the work contained in the thesis entitled *"Unstable Crack Propagation in Drawn Steel Wire, A Study on Crack Tip Plastic Flow and Effect of Warm Pre-stressing on Fracture Toughness of Mild Steel"*, by *S Sridhar*, has been carried out under my supervision and that this work has not been submitted elsewhere for a degree

DR. S. N. Bandyopadhyay

Professor

Department of Mechanical Engineering

I.I.T.. Kanpur

November, 1997.

ACKNOLEDGEMENTS

ABSTRACT

The main objective of this thesis is to understand the role of plastic zone at crack tip on mixed mode crack propagation, effect of texture in the drawn steel wire and the effect of warm pre-stressing on crack toughness Firstly, crack-path instability is studied in a drawn steel wire . Part-through semi-elliptic crack surface is observed while the crack propagates along 45^0 helical path. The maximum shear stress elevation changes its direction as the crack propagates. Secondly, unstable crack propagation is studied through shear fracture along the axis of the wire. Thirdly, the effect of anisotropy on crack tip plastic flow is studied on textured 7075-T6 aluminium alloy plate shear strain localization and non-homogeneous plastic flow produce a critical shear stress concentration on 45^0 plane. Finally, Warm pre-stressing effect has been studied in mild steel. Pre-cracked specimens are loaded in three point bend test up to the point of 60% to 95% of its fracture load at room temperature, then it is fractured at different sub-zero temperatures. Crack-toughness is seen to increase due to warm pre-stressing.

Contents

Chapter 1

UNSTABLE CRACK PROPAGATION IN DRAWN STEEL WIRE, A STUDY ON CRACK TIP PLASTIC FLOW

1.1 SUMMARY

The main purpose of this investigation is to understand the role of plastic anisotropy on crack propagation, which normally leads to an unstable fracture in textured materials. Firstly, crack-path instability is considered, in reference to, the transition for different changes in crack propagation modes 0.6 percent carbon steel drawn wire is subjected to combined mode of loading rotation in the presence of an axial tension. Mixed mode crack-propagation is observed by SEM with respect to the grain orientation direction of the wire. Part-through semi-elliptic cracks are seen to form in a wire while the crack propagates along 45^0 helical path. The maximum shear stress elevation within the plastic zone continuously changes its direction with respect to the angle of crack propagation. Secondly, an abrupt crack extension is seen to occur due to the plastic anisotropy leading to an unstable crack propagation through shear fracture along the axis of the wire.

Calculations based on Irwin-sih-smith overestimated the direction of maximum shear stress vector by 3 3^0 with respect to the axis of the wire Finally, the effect of anisotropy on crack tip plastic flow is studied on textured 7075-T6 aluminium alloy plate Experimental observation shows shear strain localization These observations favourably agree with the previous work

1.2 INTRODUCTION

Steel wires are normally made by drawing process, so that, grains are seen to be elongated along the axis of the wire Such steel wires are extensively used in engineering components. for example as valve springs, wire ropes in elevators, bicycle spokes, or even as musical instruments. In service wires are subjected to severe vibrations, obviously. producing fatigue failure. Fatigue cracks are usually seen to start from a defect on the wire surface [1 − 3]. Crack propagation mainly depends on the type of loading on the wire Final fracture occurs due to an abrupt propagation of a micro-crack along the axial direction of the wire [4 − 5]. This is mainly due to sudden loss of resistance to shear deformation along the grain orientation direction in a textured material [6]. Thus, there are three distinct stages: firstly, the initiation, which is mainly due to a surface defect secondly, the crack propagation, which depends on the type of loading, for example. a helical crack is seen to form due to a combined mode of loading under tension and torsion. and finally, micro-fracture can suddenly initiate within the plastic zone in the presense of anisotropy. (and not on the yielded-unyielded boundary, as predicted by elasticity theory [7 − 11]). It is observed that, the grain flow direction plays an important role in micro-fracture initialisation in metals.

This project is divided into three parts. The first part deals with the theoritical derivation on mixed mode loading on an inclined elastic crack in a circular wire. An explicit expression for stress intensity factor is given for a semi-elliptic part- through crack on 45^0 inclined plane [12 − 13]. Slip-line field solutions are then employed to calculate the stresses within the yielded zone. The second part is on the study of fatigue-fracture transition in 0 6 carbon cold drawn steel wire (2mm). The last part is mainly on crack tip plastic flow in heavily cold rolled 7075-T6 aluminium alloy (4 mm thin plate).

Under the action of combined mode of loading in tension-torsion, fatigue cracks were grown in wires from notch Fig. 1(a). Scanning electron microscope was found to be suitable for measuring the propagation of helical crack in steel wire (see Fig. 2(a)). Fig.

3

1(b) is a concept of plastic anisotropy in a flat plate under-tension. Fig. 2(b) shows a pin loaded aluminium specimen in tension. The tip was opened by a static load after fatigue cracking. Thin film carbon replica micro-grids were glued onto the specimen surface to measure the shear strain distribution within asymmetric plastic enclave of the crack tip. Thus, the objective of the present work is to find the reason for crack path instability in anisotropic drawn steel wires, in reference to the mode transition in crack propagation. It is observed that, at first the crack propagates in pure mode I then in a combined mode of mode I and mode II along the 45^0 plane, and finally, an abrupt mode II pure shear fracture takes place along the axis of the wire. Experiments on (7075-T6 heavily cold rolled) aluminium alloy gives an idea on the nature of plastic flow at crack tip in anisotropic material, but this may not give an exact stress field for a drawn steel wire. Hence, for an inclined crack in a wire, the reason for this sudden change in crack propagation behavior will be investigated.

Verbaak was the first to emphasize that there is a need to make such a careful study to prove the conditions favourable for an abrupt change in crack-propagation path. It is well known that an inclined crack can suddenly bifurcate under a combined mode of loading, even in an ideal isotropic elastic material. This is due to the fact that, the direction of the maximum shear stress at the tip of the crack is continuously changing as the crack propagates. Finally, the energy minimum condition has to be satisfied for an instability. Thus, there are three distinct aspects which need to be considered carefully: firstly, due to anisotropic texture, the location of the maximum shear stress elevation within the plastic zone changes as the crack propagates, secondly, due to the combined mode of loading, the direction of the maximum shear stress also changing with respect to the angle of crack orientation, and hence finally, at some stage of propagation, the direction as well as magnitude must coincide with the lowest resistance offered by the wire material to have an instability.

1.3 INCLINED PART-THROUGH SEMI-ELLIPTIC CRACK IN A WIRE UNDER MIXED MODE LOADING

One rarely finds that an initial starting crack is through the cross-section of a shaft. Figs 3(a) and 3(b) show a typical shape of a starting crack in a circular wire For the basic mathematical formulation purpose, a simplified approach has been followed as suggested by Verpoest, Aernoudt et al [5]. A semi-elliptic part-through crack is assumed to be situated on 45^0 inclined plane in a circular shaft. The co-ordinate systems are explained in Figs.3(a) and 3(c). Irwin [7], Newnan et al [12], and Smith et al [13] have analyzed this kind of problem in a rectangular beam. The stress intensity factors in Mode I and Mode II will be determined in this paper. The SIFs calculated are valid at the tip of the ellipse.

In cylindrical co-ordinate, for asymmetric situation, the equations of equilibrium, in terms of the displacements are [17 − 18]

$$\nabla^2 u + \frac{1}{1-2\nu} \frac{\partial \Delta}{\partial r} - \frac{1}{r}(\frac{2}{r} \frac{\partial v}{\partial \theta} + \frac{u}{r}) = 0$$

$$\nabla^2 v + \frac{1}{1-2\nu} \frac{\partial \Delta}{r\partial \theta} - \frac{1}{r}(\frac{v}{r} - \frac{2}{r} \frac{\partial u}{\partial \theta}) = 0$$

$$\nabla^2 w + \frac{1}{1-2\nu} \frac{\partial \Delta}{\partial z} = 0$$

where, u=radial displacement, v=tangential component of the displacement and w = axial displacement along z direction.∇^2 denotes the Laplacian operator and ν is the Poisson's ratio. Δ being the dilatation, which is given by

$\Delta = \frac{\partial u}{\partial r} + \frac{u}{r} + \frac{1}{r}\frac{\partial v}{\partial \theta} + \frac{\partial w}{\partial z}$

The equations of equilibrium are satisfied, if one takes

$$u = -\frac{\partial^2 \phi}{\partial r \partial z} + \frac{2}{r} \frac{\partial \psi}{\partial \theta}$$

$$v = -\frac{\partial^2 \phi}{r\partial\theta\partial z} - \frac{2\partial \psi}{\partial r}$$

$$w = 2(1-\nu)\nabla^2 \phi - \frac{\partial^2 \phi}{\partial z^2}$$

where, $\nabla^4 \phi = 0$, $\nabla^2 \psi = 0$

Thus, ϕ is bi-harmonic and ψ is harmonic

The stress components can be written as

$$
\begin{aligned}
\frac{\sigma_{rr}}{2G} &= \frac{\partial}{\partial z}(\nu \ \nabla^2 \phi \ - \ \frac{\partial^2 \phi}{\partial r^2}) \ + \ \frac{2}{r} \ \frac{\partial^2 \psi}{\partial \theta \ \partial r} \ - \ \frac{2}{r^2} \ \frac{\partial \psi}{\partial \theta} \\
\frac{\sigma_{\theta\theta}}{2G} &= \frac{\partial}{\partial z}(\nu \ \nabla^2 \phi \ - \ \frac{1}{r} \ \frac{\partial \phi}{\partial r} \ - \ \frac{1}{r^2} \ \frac{\partial^2 \phi}{\partial \theta^2}) \ - \ \frac{2}{r} \ \frac{\partial^2 \psi}{\partial \theta \ \partial r} \ + \ \frac{2}{r^2} \ \frac{\partial \psi}{\partial \theta} \\
\frac{\sigma_{zz}}{2G} &= \frac{\partial}{\partial z}\{ \ (2-\nu) \ \nabla^2 \phi \ - \ \frac{\partial^2 \phi}{\partial z^2} \ \} \\
\frac{\tau_{\theta z}}{2G} &= \frac{1}{r} \frac{\partial}{\partial \theta}\{ \ (1-\nu) \ \nabla^2 \phi \ - \ \frac{\partial^2 \phi}{\partial z^2} \ \} \ - \ \frac{1}{r} \ \frac{\partial^2 \psi}{\partial \theta \ \partial z} \\
\frac{\tau_{zr}}{2G} &= \frac{\partial}{\partial r}\{ \ (1-\nu) \ \nabla^2 \phi \ - \ \frac{\partial^2 \phi}{\partial z^2} \ \} \ - \ \frac{1}{r} \ \frac{\partial^2 \psi}{\partial \theta \ \partial z} \\
\frac{\tau_{r\theta}}{2G} &= \frac{1}{r} \ \frac{\partial^2}{\partial \theta \ \partial z} \ (\frac{\phi}{r} \ - \ \frac{\partial \phi}{\partial r}) \ - \ 2 \ \frac{\partial^2 \psi}{\partial z^2} \ - \ \frac{\partial^2 \psi}{\partial z^2}
\end{aligned}
$$

where, G = Shear modulus of the wire material.

One can write the biharmonic function ϕ and the harmonic function ψ in the following forms.

$$
\begin{aligned}
\phi(r, \theta, z) &= \Sigma_{m=0,1,2,}^{\infty} \ \left[\phi_m(r,z) \cos \ m\theta \ - \ \bar{\phi}_m(r,z) \sin \ m\theta\right] \\
\phi(r, \theta, z) &= \Sigma_{m=0,1,2,}^{\infty} \ \phi_m(r,z) \cos \ m\theta \\
\psi(r, \theta, z) &= \Sigma_{m=0,1,2,}^{\infty} \ \left[\psi_m(r,z) \sin \ m\theta \ - \ \bar{\psi}_m(r,z) \cos \ m\theta\right] \\
\psi(r, \theta, z) &= \Sigma_{m=0,1,2,.}^{\infty} \ \psi_m(r,z) \sin \ m\theta
\end{aligned}
$$

This is due to the fact that, considering only single valued of m, without loss of generality, one can always write $\bar{\phi}m \ = \ \bar{\psi}m \ = \ 0$

It is easily seen that ϕ_m and ψ_m are solutions of the following partial differential equations

$$
\begin{aligned}
\nabla_m^4 \ \phi_m &= (\frac{\partial^2}{\partial r^2} \ + \ \frac{1}{r} \ \frac{\partial}{\partial r} \ - \ \frac{m^2}{r^2} \ + \ \frac{\partial^2}{\partial z^2})^2 \ \phi_m \ = \ 0 \\
\nabla_m^2 \ \psi_m &= (\frac{\partial^2}{\partial r^2} \ + \ \frac{1}{r} \ \frac{\partial}{\partial r} \ - \ \frac{m^2}{r^2} \ + \ \frac{\partial^2}{\partial z^2})^2 \ \psi_m \ = \ 0
\end{aligned}
$$

Using Bessel function from snedden [18]

$$
\int_0^\infty r \ \nabla_m^4 \phi_m \ J_m(\xi r) \ dr \ = \ (\frac{d^2}{dz^2} \ - \ \xi^2) \int_0^\infty r \ \phi_m \ J_m(\xi r) \ dr \ = \ 0
$$

6

and

$$\int_0^\infty r \, \nabla_m^2 \psi_m \, J_m(\xi r) \, dr \; = \; (\tfrac{d^2}{dz^2} - \xi^2) \int_0^\infty r \, \psi_m \, J_m(\xi r) \, dr \; = \; 0$$

If one transforms w r.t. $I_m(\zeta r)$, then put $\zeta = \imath \xi$ and

$\imath^m I_m(\zeta r) = J_m(\imath \xi r)$. Let

$G_m(\xi, z) = \int_0^\infty r \, \psi_m(r, z) \, J_m(\xi r) \, dr$

and $H_m(\xi, z) = \int_0^\infty r \, \psi_m(r, z) \, J_m(\xi r) \, dr$

for $0 \leq r \leq 1$

In that case, G_m, H_m are the solutions of the partial differential equations,

$$(\tfrac{d^2}{dz^2} - \xi^2)^2 \, G_m(\xi, z) = 0 \text{ and } (\tfrac{d^2}{dz^2} - \xi^2) \, H_m(\xi, z) = 0$$

In obtaining this solution, it has been assumed that

$(r^n \frac{\partial^n \phi}{\partial r^n})_{r=1} = 0$ for n = 0, 1, 2 and 3

and $(r^m \frac{\partial^m \psi}{\partial r^m})_{r=1} = 0$ for m = 0 and 1.

where the radius of the cylinder is chosen as unity.

As ϕ and ψ are unknown arbitrary functions, a suitability chosen function can be assumed to satisfy these conditions, e.g.

$\phi = A(\theta) (\log r)^4$ or $\psi = B(\theta) (\log r)^2$ would satisfy.

The general solutions are

$G_m(\xi, z) = (A_m + B_m z)e^{\xi z} + (C_m + D_m z)e^{-\xi z}$

$H_m(\xi, z) = E_m e^{\xi z} + F_m e^{-\xi z}$

As for a long wire $z \to \infty$, the quantities must vanish, hence, the constants A_m, B_m and E_m are not admissible.

Finally, ϕ_m and ψ_m may be obtained by means of Hankel inversion theorem. However, it should be clear that the inversion is not automatic. The complex value of ξ with the substitution of $\zeta = \imath \xi$ will change the situation, in addition, because of the finite nature of integral $0 < r < 1$ the inversion will be obtained in finite range only. The final result will be obtained from an integral equation, through Stieltjes moment integral theorem.

The boundary conditions are: at r = 1, $\sigma_{rr} = 0$ and $\sigma_{rz} = 0$

After simplifying one gets,

$$D_m = 0, \; F_m = \xi C_m \text{ and also } \xi \text{ must satisfy}$$

$$\xi J_m(\xi) + \tfrac{1}{2}(m-1) \left[J_{m+1}(\xi) - J_{m-1}(\xi) \right] = 0$$

For example, when m = 1, $D_1 = 0$, $F_1 = \xi C_1$, the roots of $J_1(\xi) = 0$, $\xi = \xi_1, \xi_2, \xi_3,$. so on are the roots Thus, Snedden's theorem [26] can be applied taking sum of all the roots in the finite range inversion formula Lastly, one would get the displacements as,

$$u = \frac{1}{2} \Sigma_{m=0,1,2,}^{\infty} \left[\int_0^{\infty} F_m \, e^{-\xi z} \, \xi^2 (J_{m+1}(\xi r) \; 3J_{m-1}(\xi r)) d\xi \right] \cos \; m\theta$$

$$v = \frac{1}{2} \Sigma_{m=0,1,2,}^{\infty} \left[\int_0^{\infty} F_m \, e^{-\xi z} \, \xi^2 (J_{m+1}(\xi r) \; 3J_{m-1}(\xi r)) d\xi \right] \sin \; m\theta$$

$$w = -\Sigma_{m=0,1,2,.}^{\infty} \left[\int_0^{\infty} F_m \, e^{-\xi z} \, \xi^2 (J_m(\xi r) \, d\xi \right] \cos \; m\theta$$

The stresses can be summerized as

$$\sigma_{rr} = -2G\Sigma_{m=0,1,2,}^{\infty} \int_0^{\infty} \left[F_m e^{-\xi z}\xi^2 \{ \xi \; J_m(\xi r) + \frac{(m+1)}{2r}J_{m+1}(\xi r) + \frac{3}{2}.\frac{(m-1)}{r}J_{m-1}(\xi r) \right] \cos m\theta$$

$$\sigma_{\theta\theta} = 2G \, \Sigma_{m=0,1,2,.}^{\infty} \int_0^{\infty} F_m e^{-\xi z} \, \xi^2 \left[\frac{(m+1)}{2r}J_{m+1}(\xi r) + \frac{3}{2}.\frac{(m-1)}{r}J_{m-1}(\xi r) \} d\xi \right] \cos \; m\theta$$

$$\sigma_{zz} = 2G \, \Sigma_{m=0,1,2,.}^{\infty} \int_0^{\infty} F_m \, e^{-\xi z} \, \xi^3 J_m(\xi r) \, d\xi \; \cos \; m\theta$$

$$\sigma_{\theta z} = 2G \, \Sigma_{m=0,1,2,.}^{\infty} \left[\int_0^{\infty} F_m \, e^{-\xi z} \, \xi^3 J_{m-1}(\xi r) \; + \; d\xi \right] \sin \; m\theta$$

$$\sigma_{zr} = 2G \, \Sigma_{m=0,1,2,.}^{\infty} \left[\int_0^{\infty} F_m \, e^{-\xi z} \, \xi^3 J_{m-1}(\xi r) \, d\xi \right] \cos \; m\theta$$

$$\sigma_{r\theta} = 2G\Sigma_{m=0,1,2,.}^{\infty} \int_0^{\infty} \left[F_m e^{-\xi z}\xi^2 \{ \xi \; J_m(\xi r) - \frac{(m+1)}{2r}J_{m+1}(\xi r) + \frac{3}{2}.\frac{(m-1)}{r} \; J_{m-1}(\xi r) \} a \right] \sin m\theta$$

On $z^1 = 0$ plane, under the action of a normal pressure opening p_0 at the origin point the deflection is equal to W_0. For Mode I the sress intensity factor can be obtained from the following mixed boundary conditions:

$$w^1 = -\sqrt{2}\Sigma_{m=1,2,..}^{\infty} \int_0^{\infty} \left[J_{m+1}(\frac{\xi r^1}{2R}) - 2J_m(\frac{\xi r^1}{2R}) - 3J_{m-1}(\frac{\xi r^1}{2R}) \right] F_m(\xi)\xi^2 e^{-\frac{\xi r^1}{2R}} d\xi$$
$$\cos \; m\theta^1$$

$$= W_0 \left[1 - \frac{x_1^2}{c^2} - \frac{y_1^2}{a^2} \right]^{\frac{1}{2}} \text{ in E space (i.e. within the semi-elliptic region)}$$

$$= 0 \text{ in z - E space (i.e. in the rest of the cross-section)}$$

8

and

$$\sigma_{z^1 z^1} = -2G\Sigma_{m=0,1,2,}^{\infty} \int_0^\infty \left[J_{m-1}(\frac{\xi r^1}{\sqrt{2R}}) - \frac{m+1}{4(\frac{\xi r^1}{\sqrt{2R}})} J_m(\frac{\xi r^1}{\sqrt{2R}}) - \frac{3}{4} \frac{m-1}{(\frac{\xi r^1}{\sqrt{2R}})} J_{m-1}(\frac{\xi r^1}{\sqrt{2R}}) \right]$$
$$F_m(\xi)\, \xi^3 e^{-\frac{\xi r^1}{\sqrt{2R}}} d\xi \cos m\theta^1$$

$$= -p_0 \text{ in E space, (i.e. within the semi-elliptic region)}$$

$$= \text{unknown in z-E space, (i.e. within the rest of the wire cross section)}$$

where, the co-ordinate systems in (r^1, θ^1) are explained in Fig 3(c)

For Mode II deformation, the stress intensity factor can be calculated from the mixed boundary condition as on $z^1 = 0$ plane, proceeding in the similar manner,

$$u_r^1 = \frac{1}{\sqrt{2}} \Sigma_{m=1,3,5,.}^{\infty} \int_0^\infty \left[\frac{1}{2} J_{m+1}(\frac{\xi r^1}{\sqrt{2R}}) + J_m(\frac{\xi r^1}{\sqrt{2R}}) - \frac{3}{2} J_{m-1}(\frac{\xi r^1}{\sqrt{2R}}) \right] \bar{F}_m(\xi)\, \xi^2\, e^{-\frac{\xi r^1}{\sqrt{2R}}} d$$
$$\cos m\theta^1$$

$$= U_0 \left[1 - \frac{x_1^2}{c^2} - \frac{y_1^2}{a^2} \right]^{\frac{1}{2}} \text{ in E space}$$

$$= 0 \text{ in Z - E space.}$$

and

$$\sigma_{r^1 z^1} = 2G\, \Sigma_{m=1,3,5,}^{\infty} \int_0^\infty \left[2J_m(\frac{\xi r^1}{\sqrt{2R}}) + \frac{m+1}{2(\frac{\xi r^1}{\sqrt{2R}})} J_{m+1}(\frac{\xi r^1}{\sqrt{2R}}) + \frac{3}{2} \frac{m-1}{(\frac{\xi r^1}{\sqrt{2R}})} J_{m-1}(\frac{\xi r^1}{\sqrt{2R}}) \right]$$
$$\bar{F}_m(\xi)\, \xi^3\, e^{-\frac{\xi r^1}{\sqrt{2R}}}\, d\xi \cos m\theta^1$$

$$= -q_0 \text{in E space}$$

$$= \text{unknown in Z-E space.}$$

where, $r^1 = \sqrt{2R} - Y_1$, q_0 is the shear stress acting on the crack to create Mode II S I.F. and U_0 is the sliding displacement at the origin, of the upper face w.r.t. the lower face.

Let us first solve Mode I S.I F. problem to evaluate K_I. Thus, solving the integral equation $F_m(\xi)$ is to be determined to obtain $\sigma_{z^1 z^1}$ on $\theta^1 = 0$, at the tip of the semi-ellipse. Then a similar procedure can be followed for Mode II loading.

9

Expanding both sides on the powers of Y_1 and finally introducing,

$\int_0^\infty f(\xi)\, \xi^n\, d\xi = I_n$, with $n = 0, 1, 2, 3, 4, \ldots$

where, $f(\xi) = \xi^2\, F_1(\xi)$

for $m = 1$ i.e considering the first term in the series only, with $\theta^1 = 0$. following Titchmarsh [19], using Stieltjes moment problem,

$$F_1(\xi)\xi^2 = f(\xi) = \frac{1}{\pi\sqrt{\xi}} \Sigma_{n=0,1,2,}^{\infty} \int_0^\infty (-1)^n I_n \frac{s^{2n}}{(2n')} \cos(\sqrt{\xi}s)\, ds$$

or

$$F_1(\xi) = \frac{1}{\pi} \xi^{-\frac{1}{2}} \left[I_0\, \xi^{-\frac{1}{2}} \sin\xi + \frac{I_1}{2!}\frac{d^2}{d\xi^2}\left(\frac{\sin\xi}{\sqrt{\xi}}\right) + \frac{I_2}{4!}\frac{d^4}{d\xi^4}\left(\frac{\sin\xi}{\sqrt{\xi}}\right) + \frac{I_3}{6!}\frac{d^6}{d\xi^6}\left(\frac{\sin\xi}{\sqrt{\xi}}\right) + \cdot \right]$$

Lastly, expanding on both sides and equating the co-efficients of y_1 one can find the co-efficients I_n. Truncating upto five terms only, five linear algebraic equations will be obtained, hence, after solving,

$$I_0 = \frac{W_0}{\sqrt{2}} \left[1 - \frac{1}{4}\frac{a^2}{R^2} + \frac{1}{16}\frac{a^4}{R^4} \right]$$

$$I_1 = \frac{W_0}{\sqrt{2}} \left[\frac{3}{4}\frac{a^2}{R^2} - \frac{9}{16}\frac{a^4}{R^4} \right]$$

$$I_2 = \frac{W_0}{\sqrt{2}} \cdot 6 \left[\frac{a^2}{R^2} - \frac{1}{4}\frac{a^4}{R^4} \right]$$

$$I_3 = -\frac{W_0}{\sqrt{2}} \cdot \frac{1}{2} \cdot \frac{a^4}{R^4}$$

$$I_4 = -\frac{W_0}{\sqrt{2}} \cdot \frac{9}{17} \cdot \frac{a^4}{R^4}$$

The expressions for the normal stress on $z^1 = 0$ plane is

$$\sigma_{z^1 z^1} = -\frac{2G}{\pi} \left[A_0\, s(0,0) + A_0 S(1,0) - B_0\, z(0,-1) - B_0\, z(1,-1) \right]$$

or

$$\sigma_{z^1 z^1} = -\frac{2G}{\pi} \left[A_0\, s(0,0) + A_0 s(1,0) - B_0\, I(0,-1) - B_0\, I(1,-1) + B_0 c(0,0) + B_0\, c(1,0) \right]$$

where, $z(0,-1) = I(0,-1) - c(0,0)$ and $z(1,-1) = I(1,-1) - c(1,0)$

as well as $A_0 = I_0 - \frac{I_1}{2} + \frac{I_2}{24} - \frac{I_3}{720} + \frac{I_4}{720 \times 56}$

and $B_0 = \frac{I_1}{2} - \frac{I_2}{12} - \frac{I_3}{90} - \frac{I_4}{56 \times 144}$

The symbols for the integrals are [20]:

$$s(0,0) = \int_0^\infty \sin u\, J_0(ur_0)e^{-ur_0}\, du$$

$$s(1,0) = \int_0^\infty \sin u\, J_1(ur_0)e^{-ur_0}\, du$$

$$c(0,0) = \int_0^\infty u^{-1}(1 - \cos u)\, J_0(ur_0)e^{-ur_0}\, du$$

$$c(0,0) = I(0,-1) - z(0,-1)$$

$$I(0,-1) = \int_0^\infty u^{-1}\, J_0(ur_0)e^{-ur_0}\, du$$

$$z(0,-1) = \int_0^\infty u^{-1}\, \cos u\, J_0(ur_0)e^{-ur_0}\, du$$

$$c(1,0) = \int_0^\infty u^{-1}(1 - \cos u)\, J_1(ur_0)e^{-ur_0}\, du$$

$$= I(1,-1) - z(1,-1)$$

$$I(0,-1) = \int_0^\infty u^{-1}\, J_0(ur_0)e^{-ur_0}\, du$$

and

$$I(1,-1) = \int_0^\infty u^{-1}\, J_1(ur_0)e^{-ur_0}\, du$$

$$r_0 = \frac{1 - \frac{y_1}{\sqrt{2}R}}{1 - \frac{a}{\sqrt{2}R}}$$

From the definition of S.I.F., the mode one K_I can be determined, at the tip of the ellipse, as

$$K_I = \lim_{y \to a} \sqrt{2}\, \sqrt{y - a}\, \sigma_{z1z1} = \lim_{y \to a} -\frac{2G}{\pi}\, A_0(1 - r_0^2)^{-\frac{1}{2}}\, \sqrt{y - a}\, \sqrt{2}$$

where, $A_0 = \frac{W_0}{\sqrt{2}}\left[1 - 0.375\frac{a^2}{R^2} + 0.282\frac{a^4}{R^4}\right]$

Following Newman et al [12], after simplifying,

$$K_I = p_0\, \sqrt{\pi}\, \sqrt{a}\left[1.122 - 0.314\frac{a}{c} - 0.139(\frac{a}{c})^2 \ldots\right] \times \left[1 - 0.354\frac{a}{R} - 0.438(\frac{a}{R})^2 + 0.111(\frac{a}{R})^3\right]$$

By taking more number of terms in the series and adding higher values of m, the accuracy can be improved.

Proceeding in the same manner, for m = 1 and $\theta^1 = 0$, the stress intensity factor for Mode II can be determined, after expanding, and then equating the coefficients of y_1, one obtains similarly,

$$\bar{I}_0 = U_0\left[1 - \frac{1}{4}\frac{a^2}{R^2} - 0.663(\frac{a}{R})^4\right]$$

$$\bar{I}_1 = -U_0\left[\frac{1}{4}\frac{a^2}{R^2} + 0.272(\frac{a}{R})^4\right]$$

$$\bar{I}_2 = U_0\left[\frac{4}{13}\frac{a^2}{R^2} - 0.2314(\frac{a}{R})^4\right]$$

$$\bar{I}_3 = 0$$

$$\bar{I}_4 = 0.096\, U_0(\frac{a}{R})^4$$

11

$$\bar{I}_5 = 0$$

$$\bar{I}_6 = 0$$

higher powers of $\frac{a}{R}$ have been neglected

Thus, finally, for a Mode II shear crack,

$$\bar{A}_0 = U_0 \left[1 - 0.138 \frac{a^2}{R^2} - 0.381 \left(\frac{a}{R}\right)^4\right]$$

After simplifying, and taking limits, the stress intensity factor for a Mode II shear crack, at the tip of the semi-ellipse becomes,

$$K_{II} = q_0 \sqrt{\pi} \sqrt{a} \left[1.122 - 0.211 \left(\frac{a}{c}\right)^2 - 0.094 \left(\frac{a}{c}\right)^4\right] \times \left[1 - 0.354 \frac{a}{R} - 0.201 \left(\frac{a}{R}\right)^2 + 0.0267 \left(\frac{a}{R}\right)^2 + 0.0267 \right]$$

Accuracy can be improved taking higher order terms. p_0 and q_0 are the shear stresses acting on the semi-elliptic part-through crack.

An inclined crack under biaxial loading, the stresses near the vicinity of the crack tip are given by [15],

$$\sigma_{yy} = \frac{K_I}{\sqrt{2\pi r}} \cos \frac{\theta}{2} \left[1 + \sin \frac{\theta}{2} \sin \frac{3\theta}{2}\right] + \frac{K_{II}}{\sqrt{2\pi r}} \sin \frac{\theta}{2} \cos \frac{\theta}{2} \cos \frac{3\theta}{2}$$

$$\sigma_{xx} = \frac{K_I}{\sqrt{2\pi r}} \cos \frac{\theta}{2} \left[1 - \sin \frac{\theta}{2} \sin \frac{3\theta}{2}\right] - \frac{K_{II}}{\sqrt{2\pi r}} \sin \frac{\theta}{2} \left[2 + \cos \frac{\theta}{2} \cos \frac{3\theta}{2}\right] + \sigma(1 - K) \cos 2\alpha$$

$$\sigma_{xy} = \frac{K_I}{\sqrt{2\pi r}} \sin \frac{\theta}{2} \cos \frac{\theta}{2} \cos \frac{3\theta}{2} + \frac{K_{II}}{\sqrt{2\pi r}} \cos \frac{\theta}{2} \left[1 - \sin \frac{\theta}{2} \sin \frac{3\theta}{2}\right]$$

where, (r, θ) are usual polar co-ordinates with respect to the crack tip and crack plane, α is the crack orientation with respect to the vertical loading axis and K being the biaxial loading factor. Fig. 4(a) shows constant shear stress contour lines observed from these equations [11].

In our problem, radius of the wire = 1.0 mm, a = 0.11 mm, $\frac{a}{R} = 0.11$, $\frac{a}{c} = 0.25$ from the experimental data. Thus, if one employs the angle of initial crack extension under biaxial load conditions then from [15]

$$\left(\frac{\partial \sigma_{\theta\theta}}{\partial \theta}\right)_{\theta=\theta_0} = 0 \text{ or,}$$

$$1.75\{B_1(\alpha, K) [3 \cos \theta_0 - 1] - 3B_2(\alpha, K) \sin_{\theta_0}\} + 4B_3(\alpha, K) \sin \frac{\theta_0}{2} \cos \theta_0 = 0$$

where, $B_1(\alpha, K) = -3(1 - K) \sin \alpha \cos \alpha$ $B_2(\alpha, K) = K + (1 - K) \sin^2 \alpha$

and $B_3(\alpha, K) = (1 - K) \cos 2\alpha$

According to Verpoest [1], $\frac{q_0}{p_0} = 0.5$ on 45^0 inclined plane, then from Morh's circle, biaxiality factor $K = \frac{1}{3}$ taking $\nu = \frac{1}{3}$, after solving the above equation, one gets

$\theta_0 = 54.9^0$, which means the crack-extension is along 9.9^0 inclined with respect to the axis of the wire, which does not agree with the experiments

Following Irwin [7], Sih'[8] and Smith[9], if the strain energy density criterion is employed, then,

$$\frac{dW}{dV} r = S = a_{11}K_I^2 + 2a_{12}K_I K_{II} + a_{22}K_{II}^2$$

where, $\frac{dW}{dV}$ is the strain energy density per unit volume, which is usually expressed by

$$\frac{dW}{dV} = \frac{1}{2E}(\sigma_x^2 + \sigma_y^2 + \sigma_z^2) - \frac{\nu}{E}(\sigma_x\sigma_y + \sigma_y\sigma_z + \sigma_z\sigma_x) + \frac{1}{2G}(\tau_{xy}^2 + \tau_{xz}^2 + \tau_{yz}^2)$$

$$a_{11} = \frac{1}{16G}[(3 - 4\nu - \cos\theta)(1 + \cos\theta)]$$

$$a_{12} = \frac{1}{16G} 2\sin\theta[\cos\theta - (1 - 2\nu)]$$

$$a_{22} = \frac{1}{16G}[4(1 - \nu)(1 - \cos\theta) + (1 + \cos\theta)(3\cos\theta - 1)]$$

In order to have a crack extension Sih's [16] criterion

$(\frac{\partial S}{\partial \theta})_{\theta=\theta_0} = 0$ is to be satisfied.

For $\nu = \frac{1}{3}$, this equation simplifies as

$$\frac{K_{II}^2}{K_I^2} - \frac{4}{3}\frac{K_{II}}{K_I}\cot 2\theta_0 - \frac{1}{3} = 0$$

Solution of this equation gives, angle θ_0 at which the crack extension should occur. Taking $\frac{q_0}{p_0} = 0.5$, $\frac{a}{R} = 0.11$ and $\frac{a}{c} = 0.25$, solving the equation, $\theta_0 = 45^0 + 3.3^0$ oriented with respect to the axis of the wire. Fig. 4(b) shows this orientation angle, calculated from elasticity theory, which does not agree with experiments.

It will be demonstrated experimentally that elasticity theory alone is inadequate to describe stable crack extension in textured materials. Thus, there is a need to calculate the plastic stresses within the yielded medium in the presence of anisotropy.

1.4 CALCULATION OF PLASTIC STRESSES

This part of the paper mainly describes the method of anisotropic plastic stress calculations by slip line theory in a strain-hardening solid in the presence of non-homogeneous plastic flow In Cartesian co-ordinate, the equilibrium equations are,

$\frac{\partial \sigma_x}{\partial x} + \frac{\partial \tau_{xy}}{\partial y} = 0$ and $\frac{\partial \tau_{xy}}{\partial x} + \frac{\partial \sigma_y}{\partial y} = 0$

Hydrostatic pressure: $p = -\frac{1}{2}(\sigma_x + \sigma_y)$

Pure shear stress in yielding $K = \sqrt{\left[\frac{1}{4}(\sigma_x - \sigma_y)^2 + \tau_{xy}^2\right]}$

The direction of maximum shear stress $\phi = \frac{1}{2}\tan^{-1}\frac{2\tau_{xy}}{\sigma_x - \sigma_y}$

Hence, $\sigma_x = -p - K \sin 2\phi$, $\sigma_y = -p + K \sin 2\phi$, and $\tau_{xy} = K \cos 2\phi$

The continuity condition is $\frac{\partial u}{\partial x} + \frac{\partial v}{\partial y} = 0$

The directions of principal stress and strain must coincide,

$\frac{2\tau_{xy}}{\sigma_x - \sigma_y} = \frac{\frac{\partial u}{\partial y} + \frac{\partial v}{\partial x}}{\frac{\partial u}{\partial x} + \frac{\partial v}{\partial y}} = \tan 2\phi$

Let α and β are the well knon slip lines for a rigid-perfectly plastic solid. For strain hardening plastic solid, the third characteristics refers to the space differentiation along the direction of particle flow; the angle ψ, measured between the stream line tangent and the direction of the maximum shear strain rate direction (α). The equations referred to the characteristics for steady plane flow of a strain-hardening plastic material. the equilibrium equations are [21];

$$\frac{\partial p}{\partial \alpha} + 2K\frac{\partial \phi}{\partial \alpha} - \frac{\partial K}{\partial \beta} = 0$$
$$\frac{\partial p}{\partial \beta} - 2K\frac{\partial \phi}{\partial \beta} - \frac{\partial K}{\partial \alpha} = 0$$

Geiringers's mass continuity equations are;

$$\frac{\partial u}{\partial \alpha} - v\frac{\partial \phi}{\partial \alpha} = 0$$
$$\frac{\partial v}{\partial \beta} + u\frac{\partial \phi}{\partial \beta} = 0$$

and the hardening equation is; $\frac{h}{q}\triangle q - \sin 2\psi.\triangle K = 0$

where, $q = \sqrt{u^2 + v^2}$ = the speed of flow and ψ is the direction of flow relative to the α slip line direction,

$$\nu = \tan^{-1}\left(\frac{v}{u}\right) - \phi$$

The hardening modulus $h = \frac{2}{3}\frac{d\bar{\sigma}}{d\bar{\epsilon}} = \frac{2}{\sqrt{3}}\frac{dK}{d\bar{\epsilon}}$

These equations constitute a partially- hyperbolic quasi-linear system satisfying the isotropic hardening rule, which also implies that, the stress and strain-rate tensors are co-axial. The incompressibility condition

$\epsilon_x + \epsilon_y = 0$ is automatically satisfied

The effective strain increment is given by

$$d\bar{\epsilon} = \frac{2}{3}\left(d\epsilon_x^2 + d\epsilon_y^2 + \frac{1}{2}d\gamma_{xy}^2\right)^{\frac{1}{2}}$$
$$= \frac{2}{\sqrt{3}}\dot{\epsilon}_x \csc 2\psi \, dt = \frac{2}{\sqrt{3}}\csc 2\psi . \frac{dq}{q}$$

Thus. $h = \frac{2}{3}$ of the slope of uniaxial stress-strain curve. The effective strain may be obtained by integrating along the stream line;

$\bar{\epsilon} = \frac{2}{\sqrt{3}}\int \frac{1}{q}\csc 2\psi \, dq$

which is known as Stieltjes integral.

Hence. increment of effective strain in terms of the directional derivative of q along the streamline can be calculated from the above equations.

Now, in reference to the local axes along the streamline tangent and normal direction, this strain increment can be resolved into direct and shear components,

$d\epsilon_t = \frac{2}{\sqrt{3}}\frac{dq}{q}, d\epsilon_s = \frac{2}{\sqrt{3}}q^{-1}\cot 2\psi \, dq$

Finally $\epsilon_t = \frac{2}{\sqrt{3}}\int \frac{dq}{q}, \epsilon_s = \frac{2}{\sqrt{3}}\int q^{-1}\cot 2\psi \, dq$

The directional derivatives appearing in the equilibrium equations can be computed by numerical differentiation with suitable approximations to the arc lengths. The equilibrium equations are now integrated along the slip lines to give the mean pressure p, apart from various other additive constants. Effectively, there will be two matrices, viz., p_1 and p_2.

Therefore, the equations of rigid work hardening plasticity from a hyperbolic quasi-linear system with three families of characteristics. The third characteristic originate from the streamline.

Thus, micro-grid distortion study gives some clue how the plastic shear and dilatational strains are distributed. Chequerboard microgrid patterns, printed on the polished surface of the specimen, at the tip of an yielding crack, helps to study the non-homogeneous plastic flow field.

A simple numerical scheme has been drawn calculate the stresses, (a) Smothening of the flow pattern, (b) Computation of strain rates and the streamlines, (c) Construction of slip line mesh, and calculation of velocity field, (d) Computation of nodal points, and finally, the calculation of stresses.

The purpose of carrying out computation in this manner is not only to calculate the stresses, but also to identify the mismatch field in discontinuous deformation pattern [21] . The radial and tangential stresses are calculated from;

$$\sigma_{\phi\varphi} = K\cos 2\psi \quad \text{and} \quad \sigma_{\rho\rho} = p + K\cos 2\psi$$

Suppose that, a rigid-perfectly plastic solution is known for a given configuration, then the magnitude of the velocity jump across certain boundary will also be known, and hence, the effective shear strain jump $[\bar{\gamma}]$ is determined (where $\bar{\gamma} = \frac{\bar{\varepsilon}}{\sqrt{3}}$). In the case of hardening plastic flow, taking h as small, the change in $\bar{\gamma}$ across the strip is $\triangle\bar{\gamma} = [\bar{\gamma}]$ approximately. Hence, one gets,

$$\triangle K = \frac{1}{2}\, h \,\triangle\bar{\gamma}$$
$$\frac{\partial K}{\partial\alpha} = \frac{1}{2}(\frac{h}{b})\,\triangle\bar{\gamma}$$

where, b denotes the strip width and all quantities are to be interpreted as average of strip.

The main objective is to obtain a sufficient degree of smoothning to enable the subsequent computation of the slip line directions, as the directions of maximum shear strain rate, which in turn, can be used to construct a slip line field, for further analysis of the plastic flow. Accordingly, a maximum step size of about 0.47 μ was used, because this was the pitch line gape of the micro-grids.

The stress calculation involves estimation of the mean pressure p and the shear stress K at the slip line nodes, and their integration round a suitable path to obtain the stresses.

16

The various stages of computation are; (a) interpolation of ϵ, ϵ_x and ϵ_y onto slip line nodes, (b) determination of K and the directional derivatives $\frac{\partial K}{\partial \alpha}$ and $\frac{\partial K}{\partial \beta}$ on the basis of an experimental stress strain curve, (c) determination of the velocity field, and (d) integration of equilibrium equations

The strains are calculated as follows

$$\frac{\partial \epsilon}{\partial \alpha} = \epsilon_x \cos\phi + \epsilon_y \sin\phi$$
$$\frac{\partial \epsilon}{\partial \beta} = -\epsilon_x \sin\phi + \epsilon_y \cos\phi$$

where these directional derivatives satisfy the boundary conditions. ϵ_x and ϵ_y are the normal strain components along the direction of x and y. equilibrium equations are then integrated along the slip lines to obtain p, apart from an additional constant. Hence,

$$p = -2 \int K \, d\phi + \int \frac{\partial K}{\partial \beta} ds$$

where this integration was carried out on an α -slip line.

Thus, one would get the matrix P_2 of nodal hydrostatic pressure, similarly, a matrix P_1 is computed by integrating along β lines. Discontinuities divide the entire region into subdomains. By patching together local solutions for all subdomains, a global solution to a given boundary value problem can be constructed. In hardening flow, the slip bands do not propagate jumps in the velocity, the passage from one Hencky-prandtl net to another hardening slip line field must then include replacement of strong discontinuity, because, a real strain-hardening plastic material does not have a sharp stress discontinuity like a rigid ideally plastic solid. During stress calculations, the sharp stress discontinuity is replaced by a gradually increasing stress elevation smoothly changing over the region in a narrow band. The best possible way to do such opening a fold is to apply Whitney's theorem. Fitting a function of $p^3 + \epsilon p$, it would be possible to open the fold, provided a suitable value is taken for ϵ with proper sign. Local corner solutions with associated slip line field has been constructed from experimental observations .

A completely graphical procedure for constructing an approximate plane strain slip line field for anisotropic material is followed. The slip lines of anisotropic material under plane strain conditions are the trajectories of maximum shear strain-rate. Fig. 5(a)

shows that the α-slip line is inclined to the x-axis (in anticlockwise sense) at an angle φ. Then the outward normal to the yield locus is inclined at an angle 2ϕ to the τ_{xy} axis. Rice [22] has showen that, when referred to curvilinear α, β lines, Hencky's equilibrium equations can be integrated to give

p + s = a constant along α-line

p - s = another constant along β-line

where, p is the mean compressive pressure and S is the arc length around the yield locus, measured in the anticlockwise sense, as shown in fig 5(b)

In Figs 5(c) and 5(d) these equations have been applied around the curvilinear quadrilateral ABCD. After eliminating the pressure,

$$S_b - S_a = S_d - S_c \text{ and } S_c - S_a = S_d - S_b$$

Thus the change in the arc length between two curves of one family, at their points of intersection with a curve of the other, is the same for each intersecting curve of the second family. The details of the method of graphical construction can be obtained from Rice [22], Chitkara and Collins [23], Johnson, Malherbe and Ventor [24].

The plastic zone size can be calculated from Hill's [25] anisotropic criterion;

In general,

$$a_1(\sigma_x - \sigma_y)^2 + a_2(\sigma_y - \sigma_z)^2 + a_3(\sigma_z - \sigma_x)^2 + a_4\tau_{xy}^2 + a_5\tau_{yz}^2 + a_6\tau_{xz}^2 + 1 = 0$$

For steel wire, $\mu_1 \, \sigma_x^2 + \mu_2 \, \sigma_y^2 + \mu_3 \, \sigma_x\sigma_y + a_4\tau_{xy}^2 + 1 = 0$

Where the co-efficients are given by Mols [6] following Hill.

Therefore, inside the plastic zone, the slip line field theory proposed by Oxley [21], Hill [25] and Rice [22] for anisotropic material has been applied.

In the case of rigid-perfectly plastic isotropic material, the method of slip line can be used to determine the stresses. Henckey's equilibrium equations and Geiringer's velocity equations are used to find the direction of characteristics. In isotropic material the direction of maximum shear strain rate coincide with the slip lines, but for anisotropic material it is not so in general. The inclinations $\frac{dy}{dx}$ of the slip lines with respect to the x-axis of anisotropy can be shown to be the roots of equation;

$$(\sigma_x - \sigma_y)(dx^2 - dy^2) + 4(1 - c)\tau_{xy} \, dx \, dy = 0$$

And following the usual notation, reflecting to the slip lines as the α and β lines, the equilibrium equations can be formulated as

$\frac{p}{2T} + g(\phi) = $ constant on α -line

$\frac{p}{2T} + g(\phi) = $ constant on β -line

In the above equations, $p = \frac{1}{2}(\sigma_\alpha + \sigma_\beta) = $ the mean compressive stress, and

$g(\phi) = -\frac{\frac{c}{2} \sin 2\phi \cos 2\phi}{(1 - c \sin^2 2\phi)^{\frac{1}{2}}} + \int_0^\phi (1 - c \sin^2 2\phi)^{\frac{1}{2}} \, d\phi$

when c $=$ 0, this equation reduces to isotropic case following Henckey's relation

The velocity relation along the slip lines can be shown to be as follows;

$du - vd\phi = 0$ along an α -line

$dv - ud\phi = 0$ along a β -line

where, u and v are velocity components along the α and β lines. These are the same as Geringer's equations for an isotropic material. Fig. 5(e) describes the method of constructing slip lines in an anisotropic plastic solid.

1.5   EXPERIMENTAL

Experimental investigation on crack propagation is carried out on 0.6 percent carbon steel wire which was cold drawn with a moderate reduction to get a finished diameter of 2 mm On the contrary, crack tip plastic flow is studied on a 4 mm thickness plate, made of 7075-T6 aluminium alloy,(which normally contains 5.5% Zn in dispersed particle form). Aluminium plates are heavily cold rolled along the direction of pin-loading,(see fig 2(b)), so that, the grain flow orientations are always in parallel to the direction of tension being applied. This steel wire has an yield strength of 750 Mpa with ultimate strength as 900 Mpa, whereas, the percentage elongation at fracture is in the order of 12% The major objective of this investigation is to understand the role of plastic anisotropy on the mechanism of micro-fracture initiation within the plastically yielded crack tip region In order to study this problem, steel wires are loaded in a combined mode of tension and torsion. A fine spark-erosion cut was given on the surface of the wire to initiate a fatigue crack. Fatigueing was carried out in the presence of tension applying alternating torque in a 10 Ton Instron machine at a low cycle range (0.5 to 0.8 c/s). During fatigue cracking, $\triangle K$, as well as, axial tension, was maintained in the same way as suggested by Verpoest, Aernoudt et al [3 − 5]. After 20,000 to 30,000 cycles of fatiguing, the wires pulled in tension.

Fig. 6 shows grain flow structure of the original steel wire before loading. Grains are seen to be elongated along the along the axial direction of the wire. Figs. 7 to 11 show scanning Electron Microscope photographs for fractured surfaces of the wires, which demonstrate the presence of a fatigue crack emanating from the notch. After careful study of several samples, it is concluded that, a semi-elliptic fatigue crack surface is initiating from the wire edge. It is also observed that, this crack is trying to propagate through the wire along 45^0 plane in a helical manner. Figs. 2, 3, and 11 agree with the experimental observations of Verpoest, Aernoudt et al [3 − 5]. Thus, it is felt that there is a need to study the crack propagation behaviour of anisotropic steel wires under a combined mode of tension and torsion loading. Figs. 7 to 11 show that the fatigue

crack first starts in pure mode I; then it grows along 45^0 inclined plane through the wire in a helical manner, under the action of combined mode I and II, and finally, the crack propagates abruptly along the axial direction of the wire causing shear fracture.

Plastic stress calculations are based on the experimental study on flow pattern in 7075-T6 aluminium alloy. Fig. 12 explains the role of slip lines ahead of a notch under a pure bending action. This is taken from Cottrell and Knott [26], Green and Hundy[27], Hill [25] and Johnson, Sowerby et al[28]. Fig. 13 explains the formation of a plastic zone at crack tip in 7075-T6 aluminium plate. This shape (in Fig. 13) is observed by a Differential Interference Contrast microscope on the surface of a pin-loaded tension specimen (see Fig. 2(b)) at 8.34 KN static load. To study slip line formation within the plastic zone SEM observation was found to be very suitable. Figs. 14 to 16 confirms the presence of shear lines within yielded zone, hence- forth, will be called as slip lines. These shear lines are carefully drawn to understand the slip systems within the plastic enclave ahead of an yielding crack tip. Fig. 17 shows the asymmetry in the plastic zone shape due to anisotropy, and also describes the nature of slip line formation regions. This kind of slip line plot is entirely based on the experimental observations on 7075-T6 aluminium alloy The next step is to see how Sih's model [29] operates within the plastically yielded enclave. If one assumes that a crack tip model can be simplified as an incompressible plastic medium, fitted into a cut-out empty space in an elastic plate, then shrink-fit type on-load plastic stress within the enclave can be studied by a simple photoelastic model. Fig. 18 shows an incompressible polyurethene rubber ($\nu = 0.5$) fitted into a cut-out space inside a CR-39 photoelastic plate ($\nu = 0.34$). Not only both the materials were made stress free initially, but also, after joining, they are again made stress free. The bonding was perfect, having no residual or shrink-fit stresses present due to araldite adhesive joining. In Fig. 18,approximate dimensions are: maximum horizontal width of the rubber insert= 25.4 mm, minimum depth of the rubber insert under the vertical slit = 4.0 mm. Depth of the CR-39 plate = W = 55 mm, span = 4 W, thickness of CR-39 plate = 6 mm, vertical slit length of the cut = 10 mm, load applied = 99 N under three point bending. Fig. 19 explains the contour lines for constant

shear stress obtained from isochromatic fringes. The geometry of the poly- eurethene rubber insert has been chosen close to the plastic zone shape normally seen in a metal. Photoelastic experiment would certainly help to understand the differential mismatch stress (e g shrink fit stress type), created within the enclave Fig. 19 clarifies that there are two distinct regions within the enclave. "Region A" is mainly due to the differential compression on the crack extension plane arising out from the boundary contraction below the slit. Point B in Fig. 19 gives a pure shear region, which is mainly due to the combined action of horizontal sidewise and vertical compression. This type of strain field is due to tension-compression changing region, commonly seen at the center of a bending bar. Thus. "Region B" of Fig. 19 is due to a pure distortion, which agree with Sih's model [29].

Figs. 20 to 23 show printed (or marked) grid patterns on crack tip surface in 7075-T6 aluminium alloy specimens. Firstly, fatigue crack was grown at $K_I = 9Mpa\sqrt{m}$ in a pin- loaded tension specimen of 7075-T6 aluminium alloy (see Fig. 2(b)). Secondly, the specimen was pulled in tension to see the crack opening as well as plastic flow. Finally, grid distortion was observed under a differential interference contrast microscope as well as on scanning electron microscope. Photo offset grid patterns are made at Agfa-Ghobert factory at Mortsell, Belgium with grid size as 24μ,which was found to be inadequate to understand the flow field within the yielded medium. Micro- hardness indentation marks were made on the surface of aluminium alloy plate with a size of 6.5μ as diagonal length using 136^0 diamond pyramid indentor in Leitz microscope. Figs. 21 to 23 show that $6 5\mu$ grid was also inadequate. Although, in the previous work, laser beam marking was employed with 0.6μ pitch distance [30], this time transmission electron microscope calibration piece supplied by polaron Co., England was directly put on the crack tip to measure plastic strain. These micro-grids are on a thin film carbon replica which is mounted on a copper foil mesh as a support. such calibration grids are fixed onto the crack tip by Silastic rubber (silicon type) bonding glue. A very thin layer of glue was put on the surface of the specimen, so that, a large plastic strain can be accommodated on the replica. Fig. 24 shows SEM photograph for such polaron micro-grids, having a

dimension of 0.47μ as pitch distance between the two consecutive lines, and 0.06μ as line thickness. Fig. 24 is taken when no load was on the specimen. Fig. 25 shows micro-grid distortion at crack tip due to 8.34 KN tension load on the sample. Radial flow pattern below the tip is confirmed from Fig. 25, which means, metal extrudes out from the root of the crack. Fig. 26 shows a micro-grid distortion pattern on 45^0 plane, giving a shear deformation. Shear strain distribution is calculated from these figures. The crack was further loaded to 11 KN and again micro-grid distortion was recorded at different regions. Figs. 27 and 28 show such grid distortions, which would certainly help to calculate strains on the plastically yielded zone. Fig. 29 shows more radial plastic flow at higher load, before the onset of fracture. Thus, from these photographs, it is clear that, extrusion and intrusion of metal play the most important role in micro-crack nucleation. Fig. 30 gives strain localisation within the plastically yielded medium ahead of a crack tip. Such non-homogeneous plas tic flow is seen to occur at a higher load, before the onset of crack extension. Shear bands are seen to form within the plastic zone. Local strain concentration is also visible from Fig.30. Intrusion-Extrusion of metal must be responsible for such type complex folding deformation. Strain distribution has been measured within the shear band. Such flow-localization creates stress concentration ahead of an yielding crack tip [30 − 33]. Fig. 31 has been taken at 18000X magnification at crack tip. Hence, it is possible to measure all the three components of plastic strain at a point on the surface of a crack tip. This study has certainly helped to understand non-homogeneous plastic flow in an anisotropic material.

1.6   DISCUSSION

Our experimental investigation, described in Figs. 7 to 31, has one thing in common that always there will be a shear strain localisation within the plastic enclave, before the onset of abrupt crack extension.

Photoelasticity experiments (mentioned in Figs. 18 and 19) as well as micro-grid distortion recorded on aluminium alloys (see Figs. 25 to 31) have certainly helped to

understand the complex strain field inside a plastic zone, particularly when, there is a mode transition in crack propagation for a textured material Experimental investigations on crack propa gation on 0 6μ carbon steel wire, and crack tip strain measure ments in aluminium alloy also explain the role of grain flow direction on micro-fracture initiation in steel Figs. 7 to 11 further elaborate, the transition in crack propagation modes. for drawn steel wires, which were fractured after giving a number of cyclic loading in a combined mode of tension-torsion.

Recently, attention has been focussed on the propagation of an inclined crack under combined mode of loading [10, 11, 13, 15and16], but plasticity aspect has not been considered properly, especially, in the background of new development on stable crack extension theory. This work may help to under stand sub-critical crack growth for an inclined crack in a textured metal. Although, Irwin-Sih-Smith approach [7 − 9] has helped to find conditions favourable for crack-extension in elastic materials (like polymer, rubber or glass), unfortunately, such calculations may not be aplicable in metals, especially without any previous knowledge on plastic stresses or anisotropic grain flow conditions. Stress concentration due to strain- localisation makes the situation more intresting, in the presence of anisotropy. Non-homogeneous deformation and reverse plastic flow with shear localisation within the plastic zone are seen to occur. Figs. 7 to 11 demonstrate abrupt crack-path instability for one inclined crack in a steel wire, because of anisotropy.

For a cold drawn steel wire, a crack initiates purely in mode I (see Figs. 10 and 11) as expected, and then, propagates in a combined mode with Mode I and mode II. Fig. 11 shows that the crack- growth is seen to occur along 45^0 plane in a helical manner under combined mode [1]. For ths 45^0 inclined semi-elliptic crack, it is emphasized that the shape of the plastic zone will always be asymmetric. This is mainly due to the mixed mode loading on the crack and plastic anisotropy [6, 11, 15] (see Figs. 4(b) and 11). Next, two distinct conditions are to be satisfied: firstly, one of the 'rabbit shear-edr' of plastic enclave should be parallel to the axis of the wire, and secondly, a critical shear stress concentration would be needed within the plastic zone [30 − 34]. Thus, at some stage of the growth, this inclined semi-elliptic crack suddenly bifurcates along the

axial direction of the wire This is mainly due to the sudden loss of resistance to shear deformation parallel to the axis of the wire, and happens to be the anisotropic grain orientation direction of the texture Such unstable crack growth can easily be observed, if the resolved components of stresses are chosen in such a manner, so that, on 45^0 inclined plane, the applied shear stress is half of the normal stress being applied [1], i.e $g_0 = 0\ 5p_0$.

Our calculation based on elasticity theory suggests that a 45^0 inclined semi-elliptic crack should extend along a direction of 8.3^0 with respect to the axis of the wire. However, experimental observations (see Figs. 7 to 11) on steel wires do not agree with this The discrepancy is due to the fact that , neither $(\tau_{max})_{\theta=\theta_0})$ is a critical shear stress concentration at crack tip for a metal, nor crack would ever nucleate at the elastic-plastic boundary. The objective of this work is to prove that , in order to have a crack extension, the local maximum shear stress vector within the yielded zone must coincide with the direction of anisotropic texture

In a drawn steel wire, not only one should know, the asymmetric shape, size and orientation of the plastic zone for an inclined crack, but also, it is equally important to determine the maximum shear stress concentration and its direction with respect to anisotropy. A simplified approach based on the findings on aluminium alloy has been presented here, because, it was not possible to put micro-grid on a steel wire. Figs. 27 to 31 give more non-homogeneous plastic flow due to anisotropy, compared to our previous investigation on isotropic 7075-T651 aluminium alloy [30]. Figs. 32 presents the final result for for the shear stress concentration on 45^0 plane, ahead of an yielding crack tip in 7075-T6 aluminium. A possible slip line field is conceived in Fig. 33 [30].

Thus, for an inclined crack in a wire under combined mode of tension torsion abrupt change in the direction of crack propagation path is due to the following reasons: firstly, one of the "rabbit ears" of the plastic zone must orient itself along the axial direction of the wire, secondly, the resolved maximum shear stress concentration on 45^0 plane, within the plastic zone, must reach at the critical value, and lastly, at some suitable point inside the material, during a favourable stage of propagation. the magnitude as

well as the direction of this maximum shear stress must coincide with the minimum resistance to shear deformation offered by the anisotropic wire
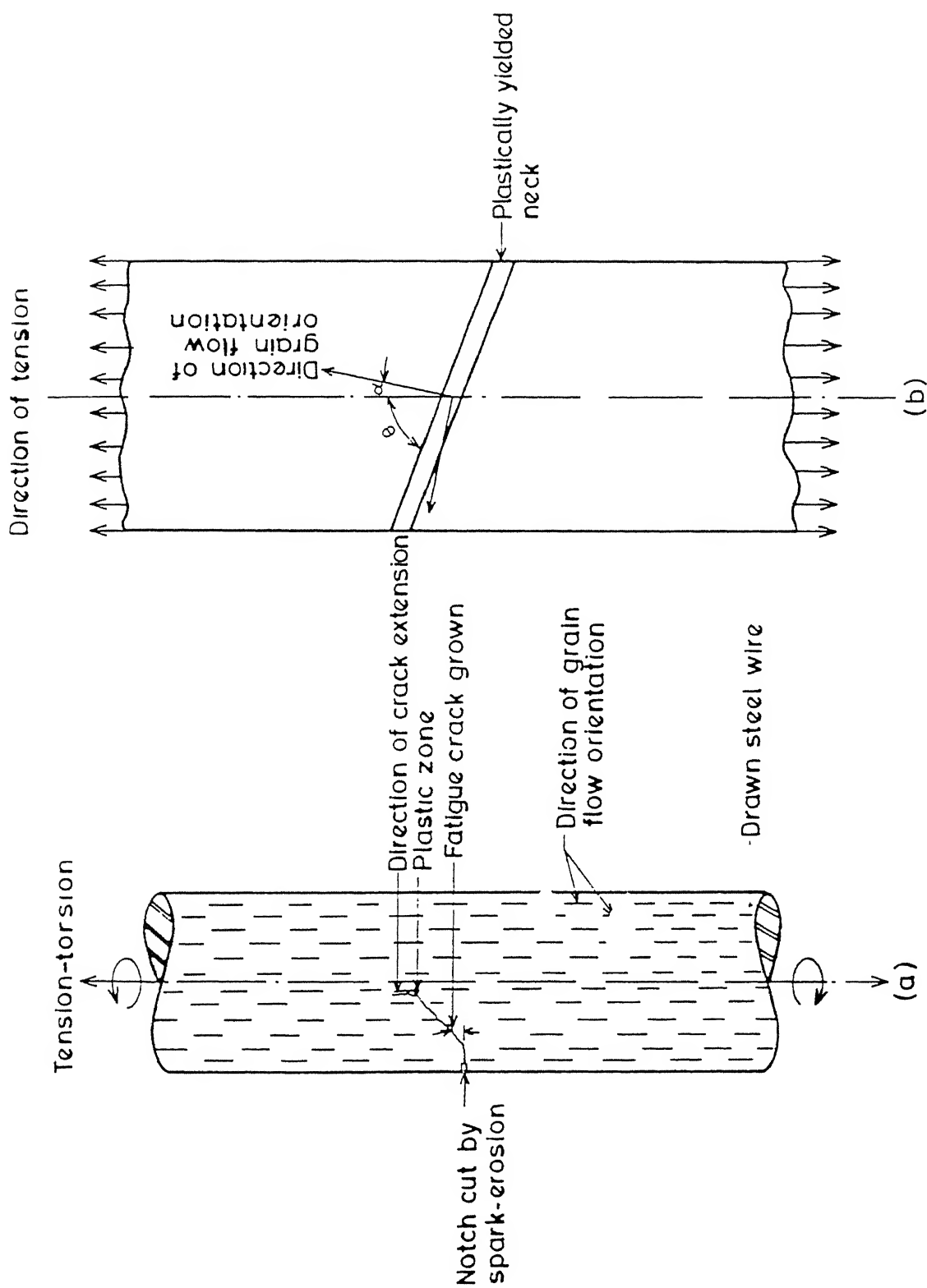
Fig. 1(a) Cold-drawn cylindrical steel wire of 2 mm dia under combined mode of loading in tension and torsion. Grain flow direction is parallel to the wire axis A spark erosion 0 1 mm notch cut is given at the middle length of the wire, as fatigue crack starter

Fig. 1(b) Oblique necking in a strip under tension [25]. Direction of grain flow is not parallel to the direction of tension loading Material, 7075–T6 aluminium alloy plate

Fig 2(a) Semi-elliptic crack on 45° inclined plane in a steel wire, which is growing in a helical path.

Fig. 2(b) Dimensions for a typical pin-loading type tension specimen as per ASTM Material, 7075-T6 aluminium alloy. Grain flow direction is parallel to the tension loading axis

28
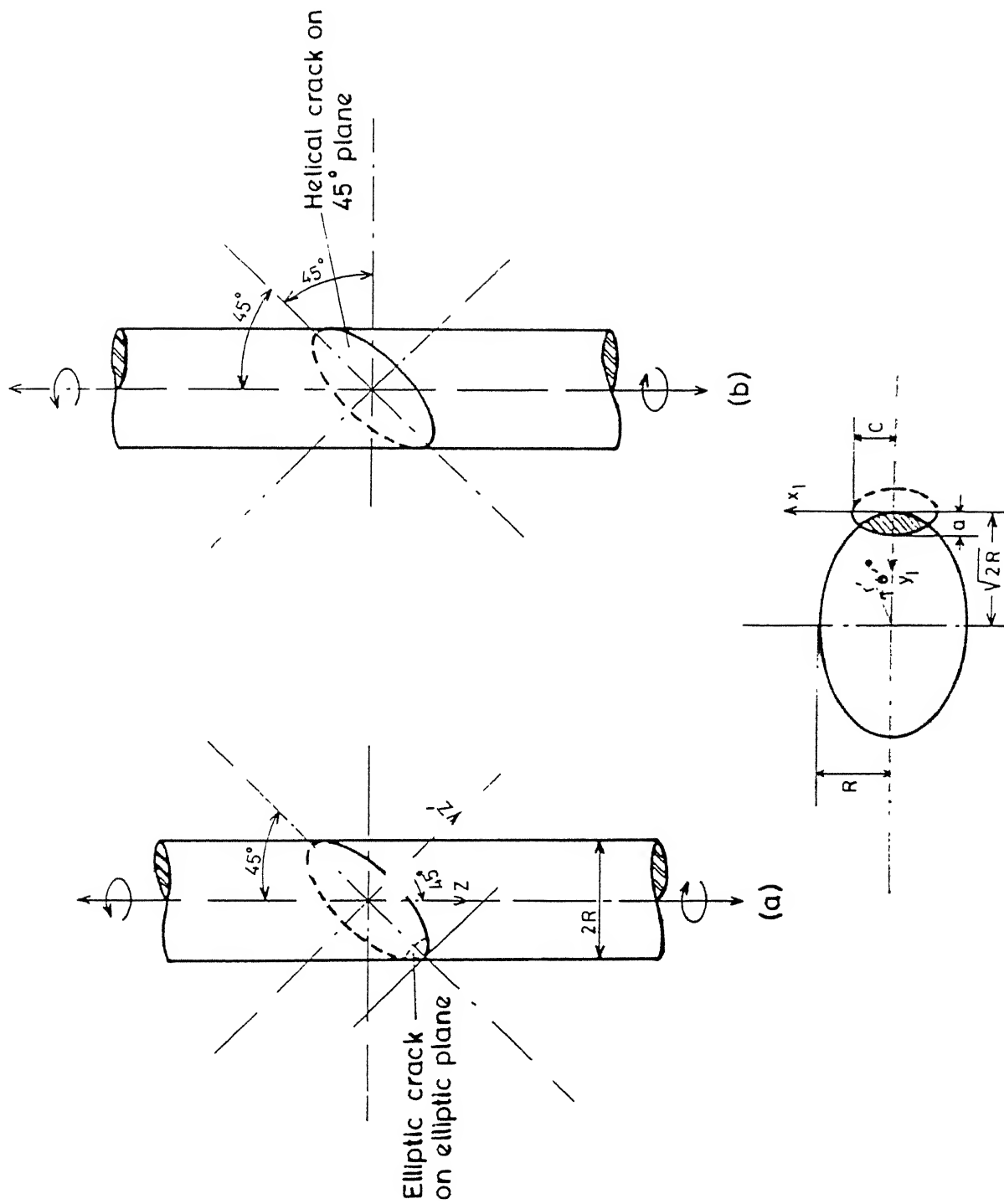
Fig. 3(a) Co-ordinate systems for semi-elliptic crack on elliptic plane are described

Fig. 3(b) Angle of orientation of the elliptic plane with respect to the wire axis is explained

Fig 3(c) Co-ordinate systems on inclined plane are described.

29
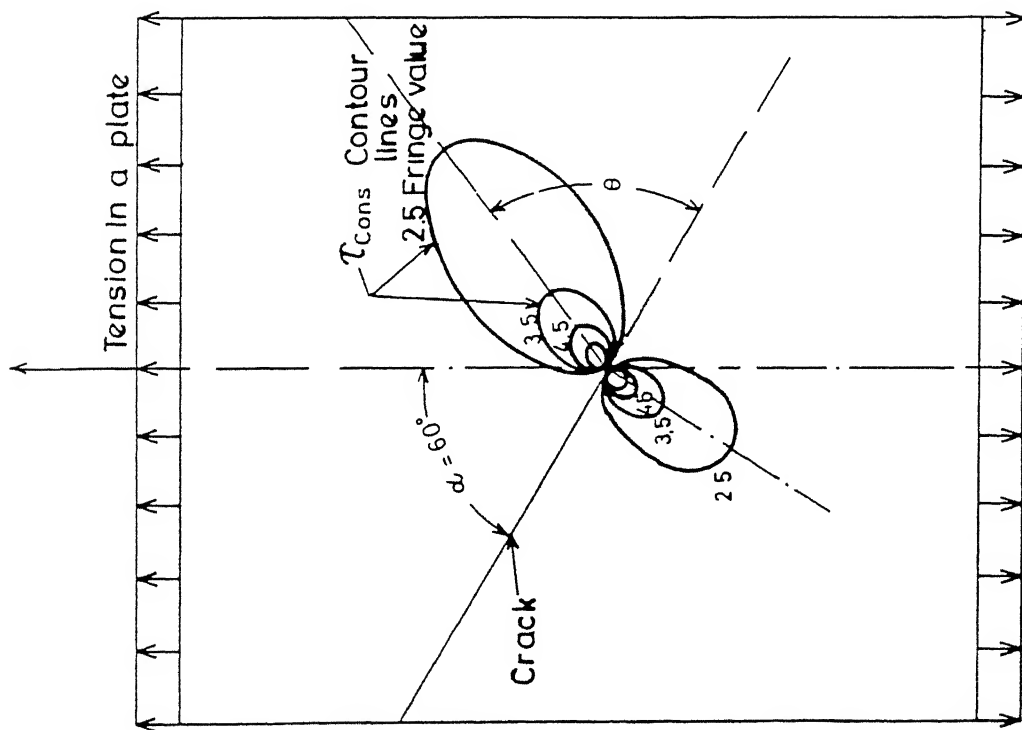
Fig. 4(a) A 60^0 inclined crack is in a tension plate. Constant shear stress contour lines are calculated from References [11, 15, 16] to obtain photo elastic data for different fringe values

Fig 4(b) Plastic zone formation is explained at the tip of an inclined crack in a circular wire τ_{max} at $\theta = \theta_0$ is also shown Irwin-Sih elastic theory suggests that the angle of crack extension should be at 3.3^0 with respect to the axis of the wire
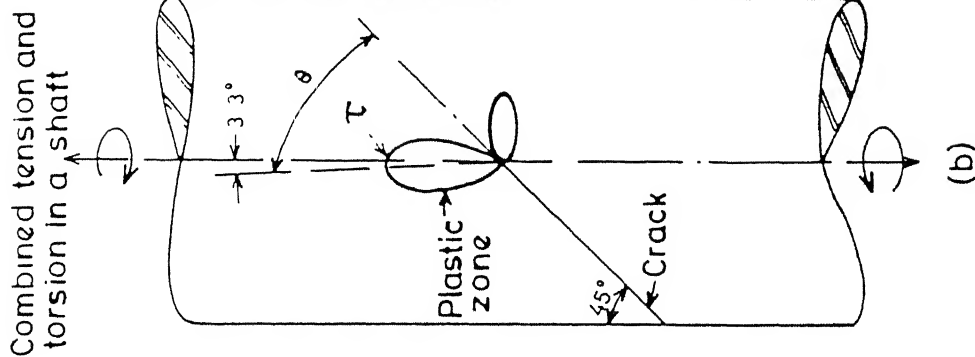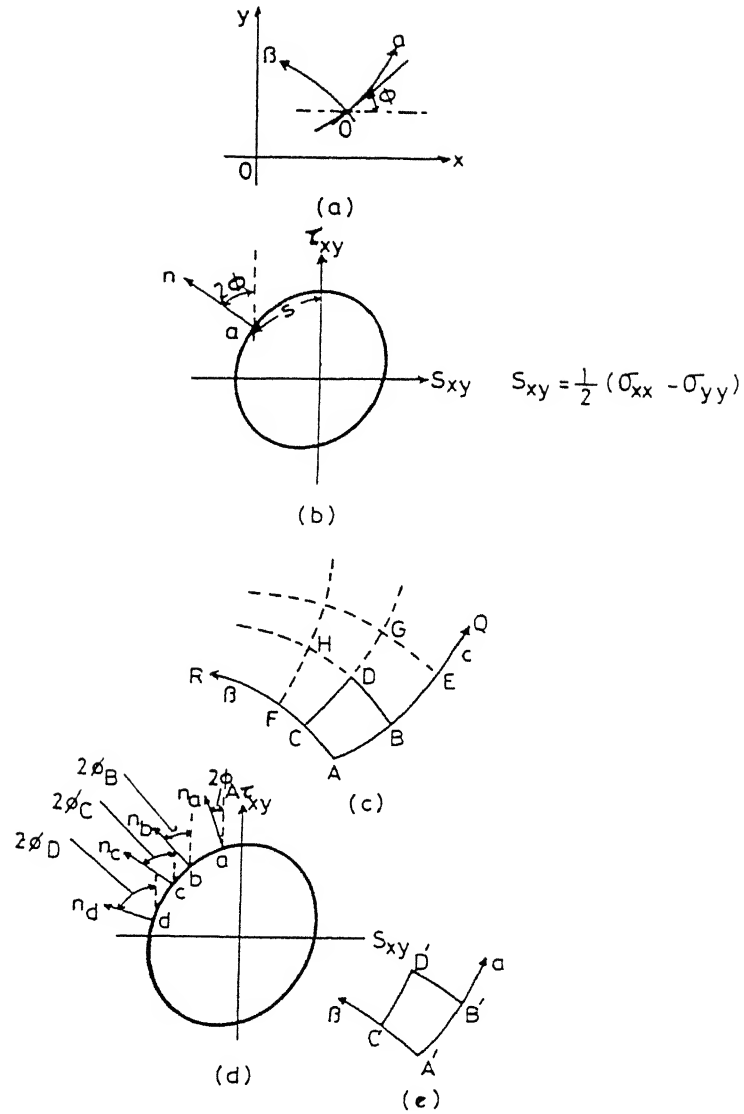
Fig 5(a) Relation between the slope of slip-lines and normal on yield locus [23].

Fig 5(b) Arc length measured on the yield locus.

Fig 5(c) Slip line construction by graphical method.

Fig. 5(d) Variation of angle ϕ on the yield locus at different net points.

Fig 5(e) Final modified shape of the slip net along α and β directions.

31
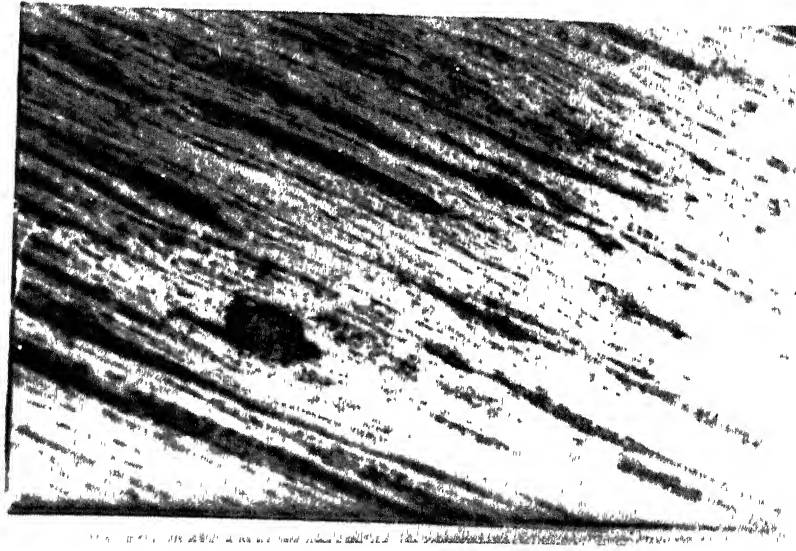
Fig. 6 Grain flowstructure for 0.6 C steel wire, obtained after cold drawn through the HSS die. Grains are seen to be elongated along the axis of the wire.

Fig 7 A typical helical fractured surface of a wire after fatigue cracking. Scanning
Electron Microscopic observation at low magnification.
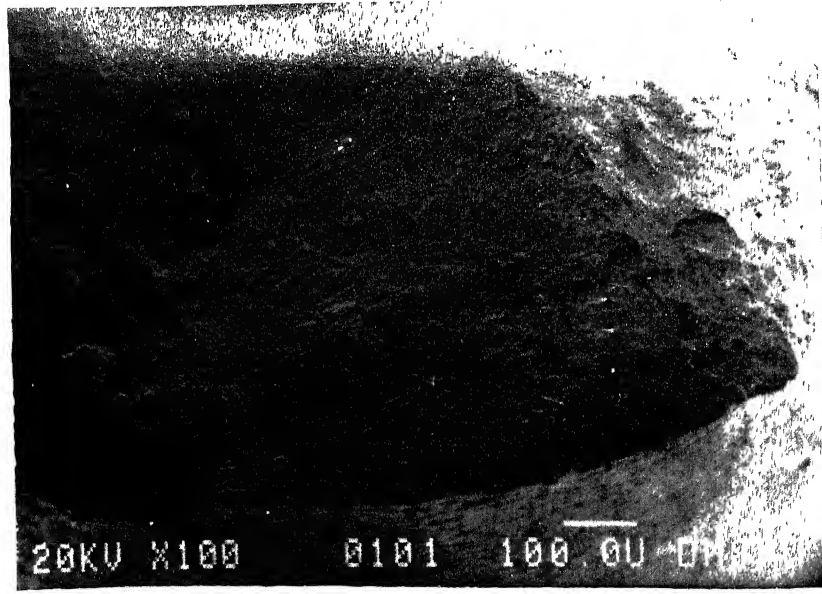
Fig 8 SEM photograph showing different fracture surfaces in a 2 mm steel wire.
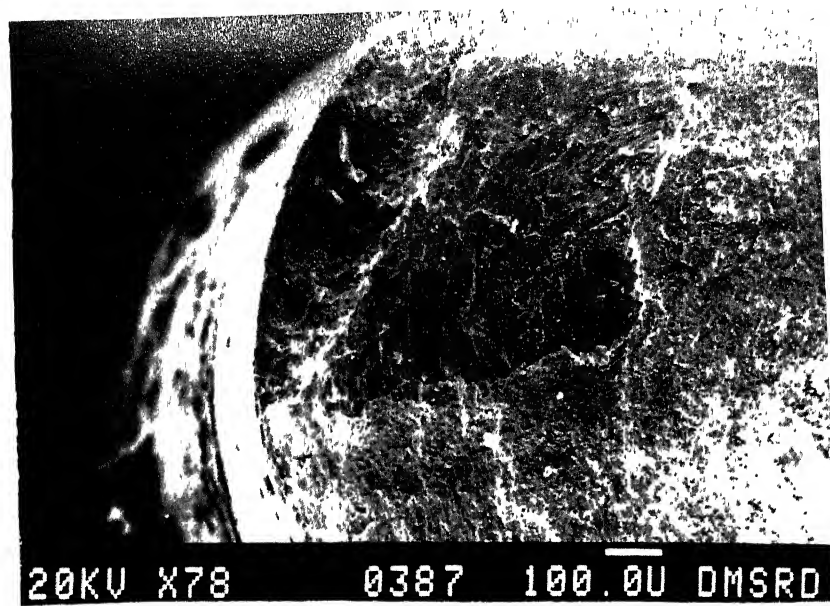
Fig 9 SEM photograph taken at an angle showing different fracture surfaces for a 2 mm steel wire.
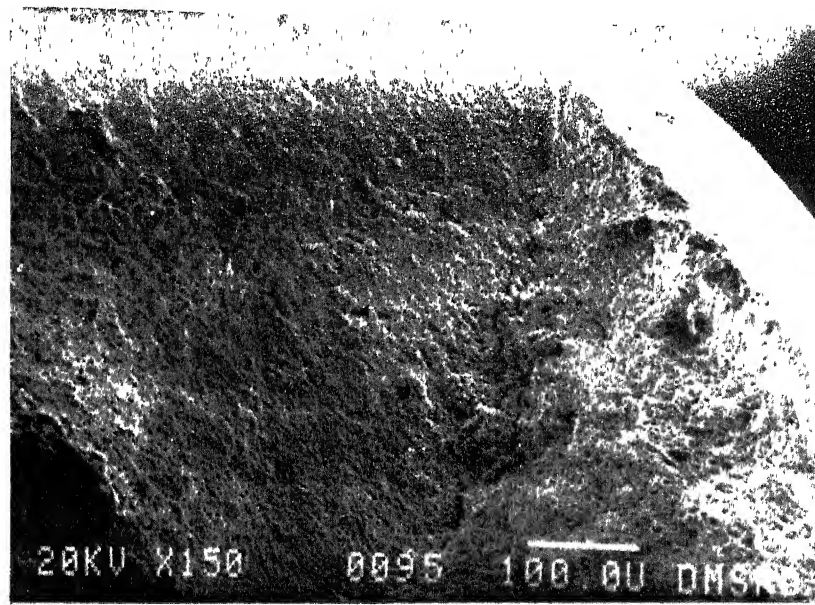
Fig 10 SEM photograph showing the initiation of a surface fatigue crack from spark notch cut.
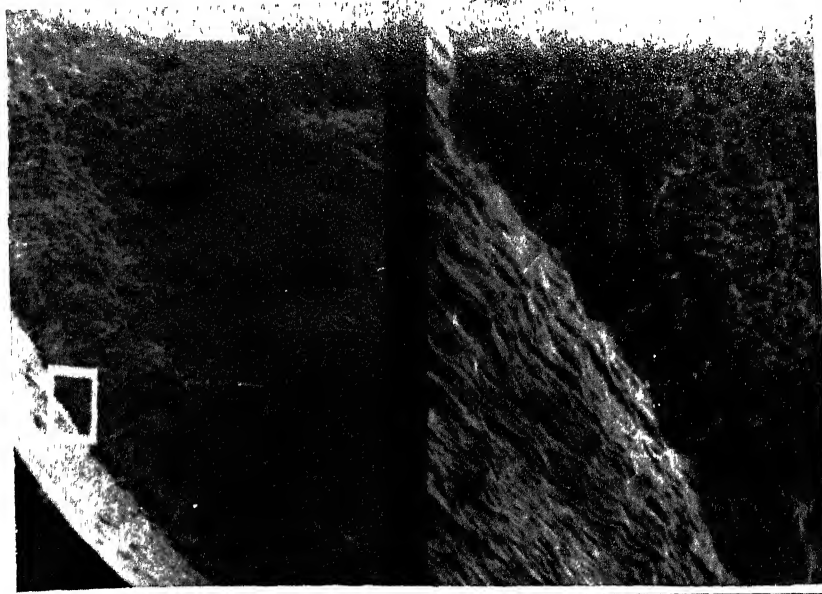
Fig 11 Same SEM photo of FIg 10 on the right hand side, but a small region is magnified X10 times more than the right hand side. showing fatigue crack on the L.H.S. figure. A semi- elliptic crack is forming on elliptic plane inside the wire [5] . conditions for the crack growth is taken from Ref [5]. but grown in a low cycle fatigue machine. $\triangle P_{axial} = 0 \ 1 P_{fracture}$, $\triangle T = 0.85 \ T_{fracture}$, $N = 28,000$ cycles, where T is torque and P is the axial load on the wire
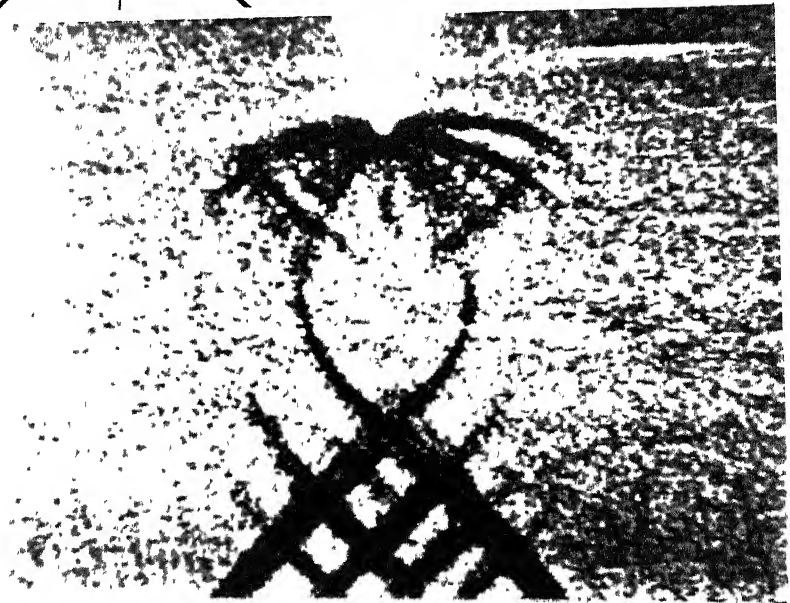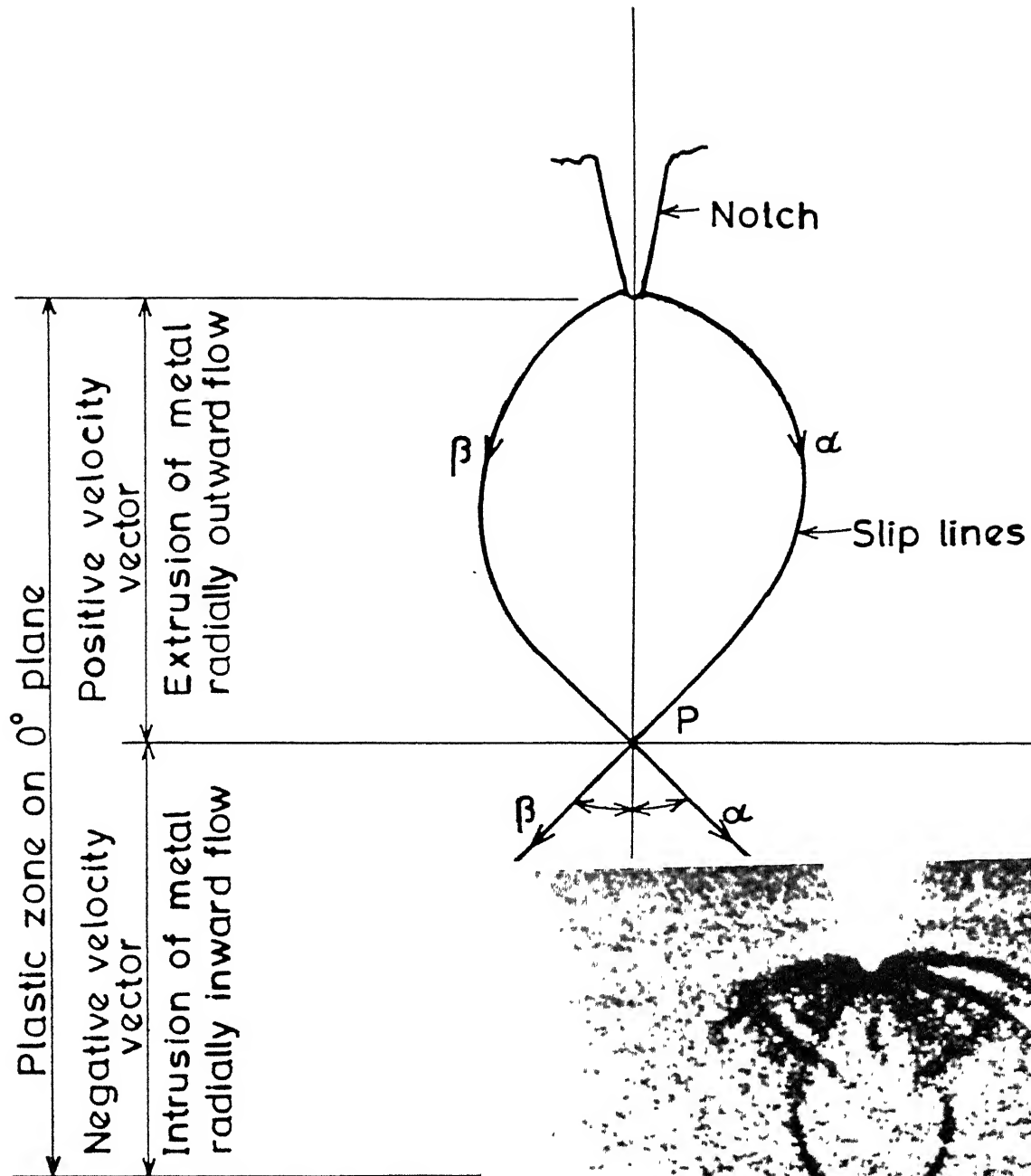
Fig 12 Slip line field from a deep groove V-notch under pure bending action on the beam. Experimental observation by Fry's reagent on Nitrogenated steel is also shown on a photograph [25 − 28].

38
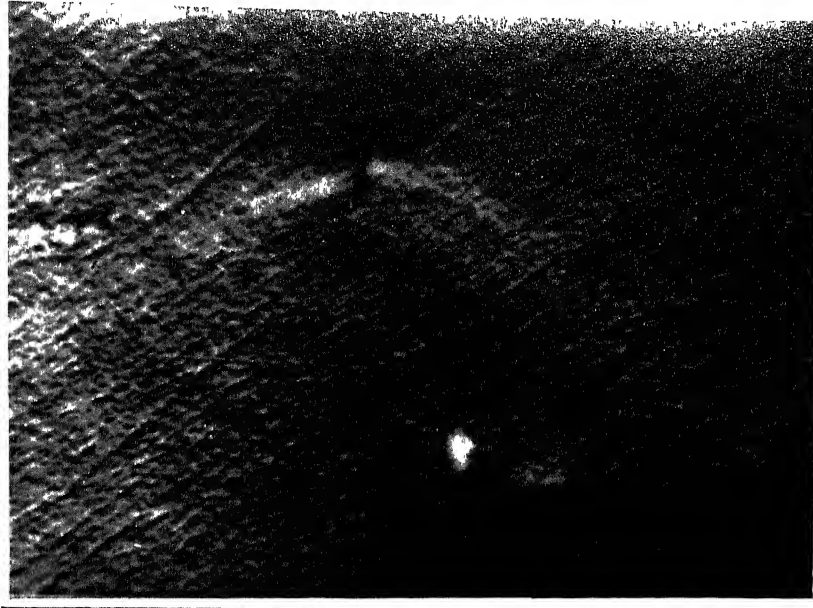
Fig 13 Plastic zone measured on the surface of 7075-T6 aluminium fatigue cracked beam. Photograph was taken in a Differential Interference Contrast microscope. Crack size = 3 41 mm. Pin loaded tension specimen. Load applied = 8.34 KN. Pre-cracking for fatiguing $\triangle K_I = 9 Mpa \sqrt{m}$ with R = 1 $\triangle K_{Ic} = 27 Mpa \sqrt{m}$

Fig.14 Slip systems observed at crack tip by SEM study. conditions are same as Fig. 13 Material; 7075-T6 alumınıum.
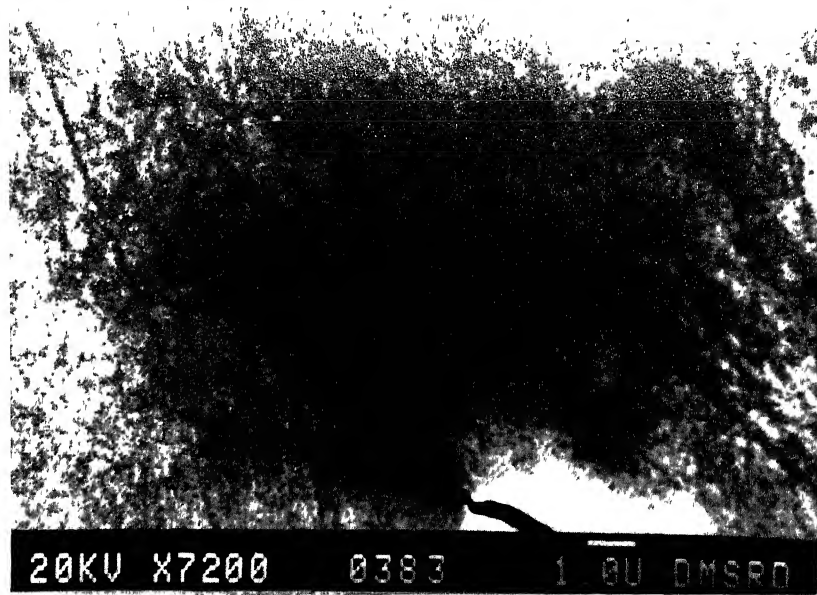
Fig.15 Same slip systems observed at crack tip of Fig. 14, but a higher magnification (7075-T6)
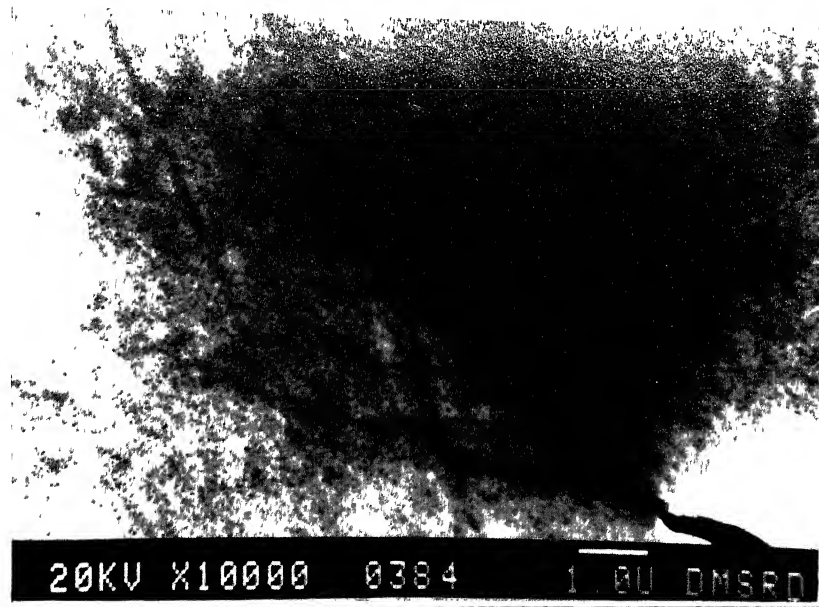
Fig 16 Slip systems of Figs. 14 and 15 observed at a further higher magnification (7075-T6)
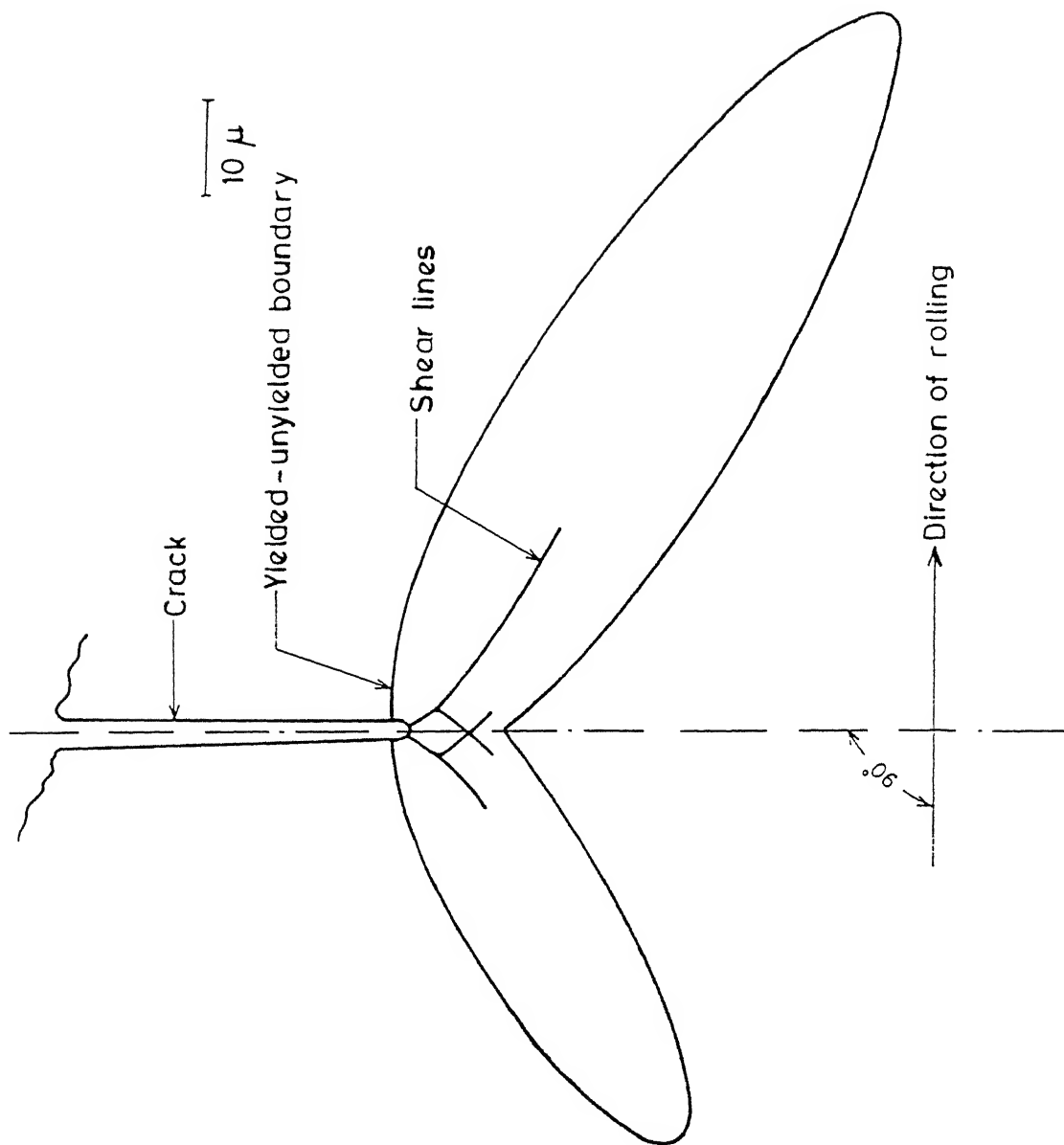
Fig.17 Yielded-unyielded boundary is plotted to scale showing the shape and size of the plastic zone in 7075-T6 aluminium alloy fatigue cracked plate. conditions are same as Fig 13. This is obtained from the observations of Figs. 12 to 16 Asymmetric shape due to the presence of anisotropy is clear Bending field is present
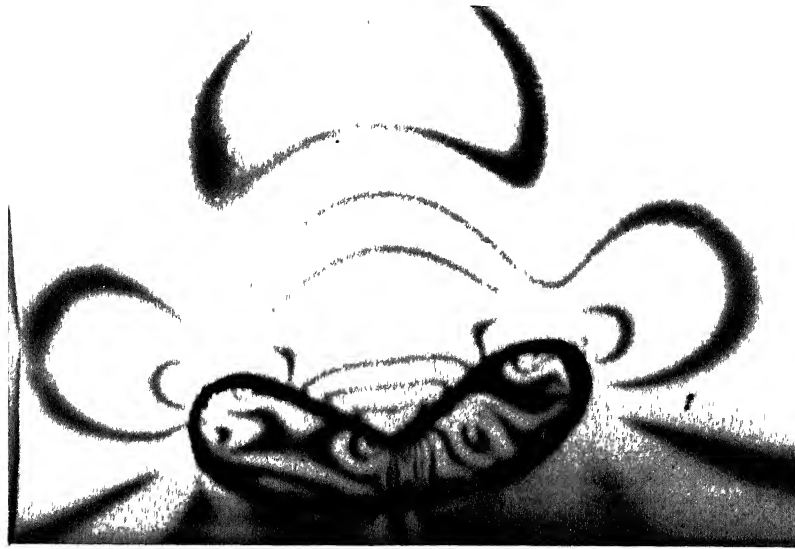
Fig.18 Photo-elastic isochromatic fringe pattern is shown inside polyurethene rubber insert, fitted inside a CR-39 photoelastic matrix. Differential mismatch loading is clear inside the rubber insert. Load = 99 N, 3 point bending loading, CR-39 specimen sizes are W = 55 mm, S = 4W, B = 6 mm, L = 250 mm, slit size = 10 mm minimum insert depth under the slit = 4 mm and the maximum width of the rubber insert = 25.4 mm.
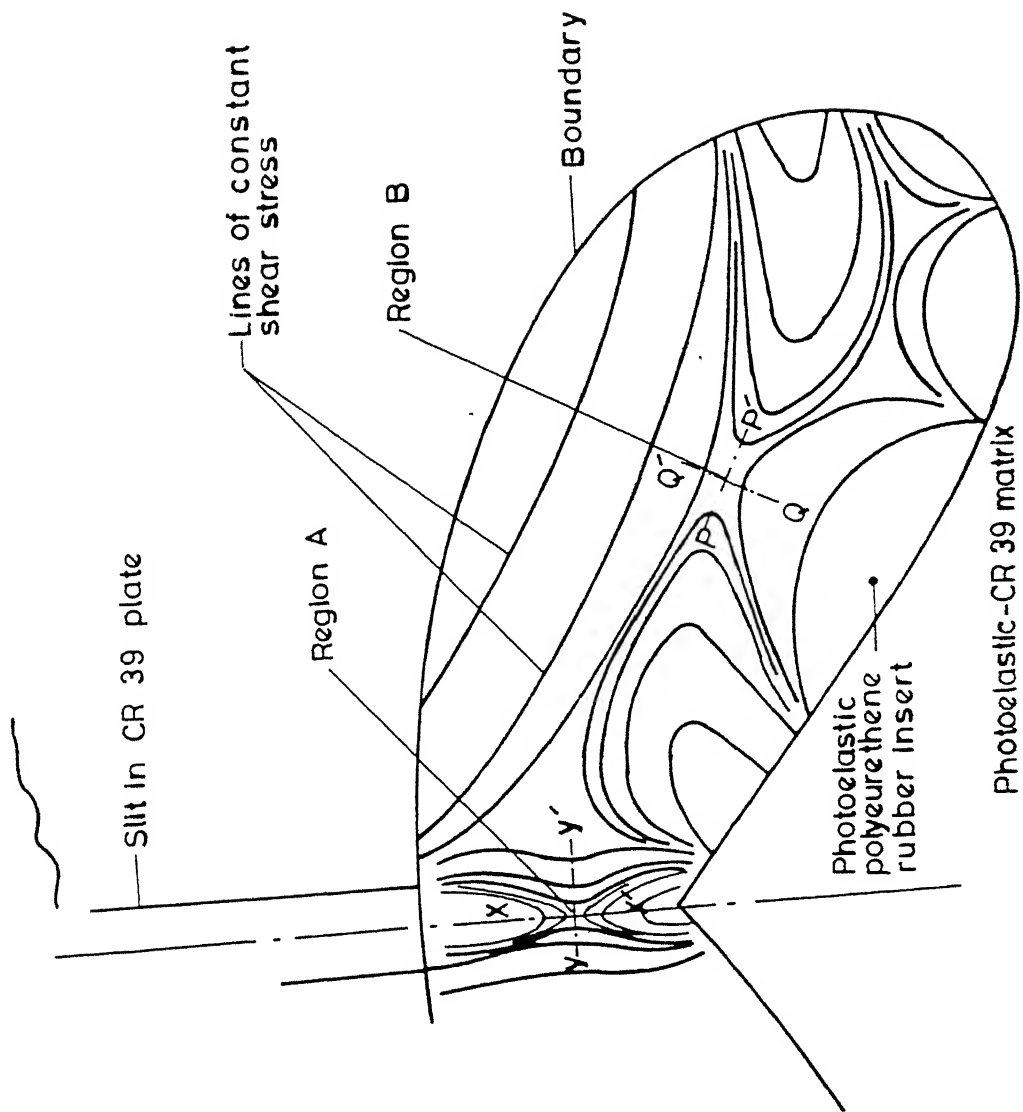
Fig.19 Constant shear stress lines inside the rubber insert due to differential mismatch boundary movement. 'Region A' demonstrate the presence of a differential compression, whereas. 'Region B' confirms a pure shear field due to bending and side-wise compression. This helps to understand the slip lines inside plastic enclave. This agree with Sih's model[29] in metals.

45
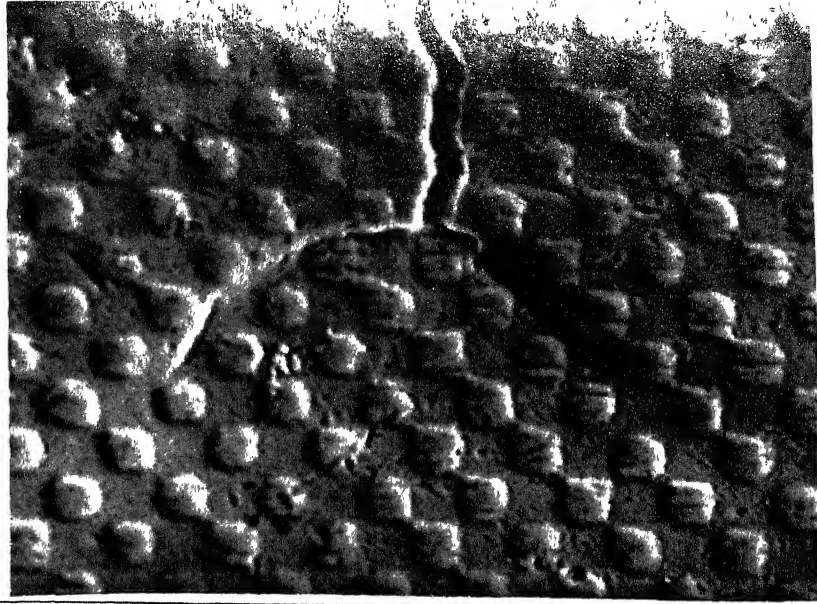
Fig.20 grid distortion study at crack tip, before the onset of fracture. Grids were made by photo-offset technique at Agfa-Gobert, Mortsell, Belgium. Size of each square grid = 24 μ mesh. Material; 7075-T6 aluminium alloy. Crack size = 3.69 mm. Pin-loaded tension specimen. Load applied = 1250 KN Fatigue pre-cracking data $\triangle K_I = 9 Mpa \sqrt{m}$ with R = 0.1.
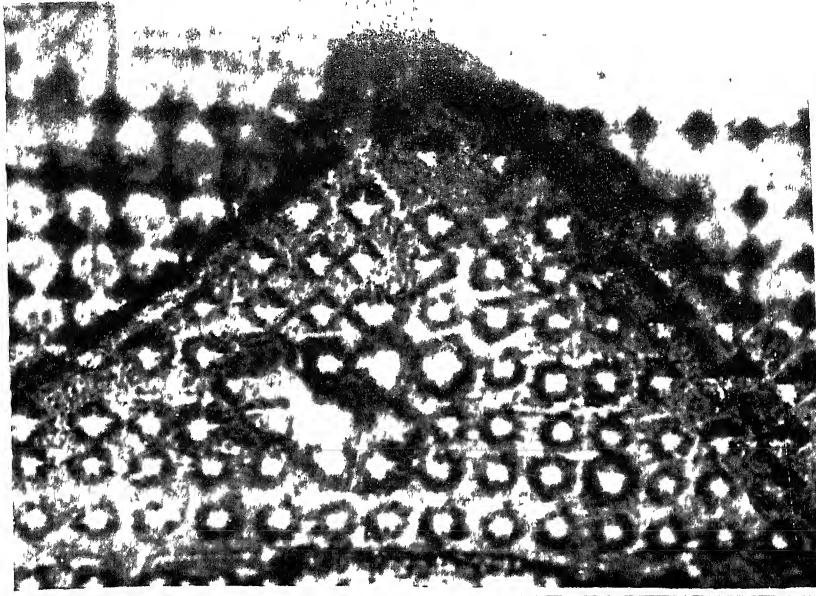
Fig 21 Grid study on the surface of a 7075-T6 aluminium alloy specimen (by Leitz micro-hardness tester) indentations. Grid sizes = 6 5 μ, pitch between the consecutive grid centers = 10 μ. Crack size = 3.69 mm. Pin-loaded tension specimen. Load applied = 11 KN. Fatigue cracking at $\triangle K_I = 9Mpa \sqrt{m}$ with R = 0.1.
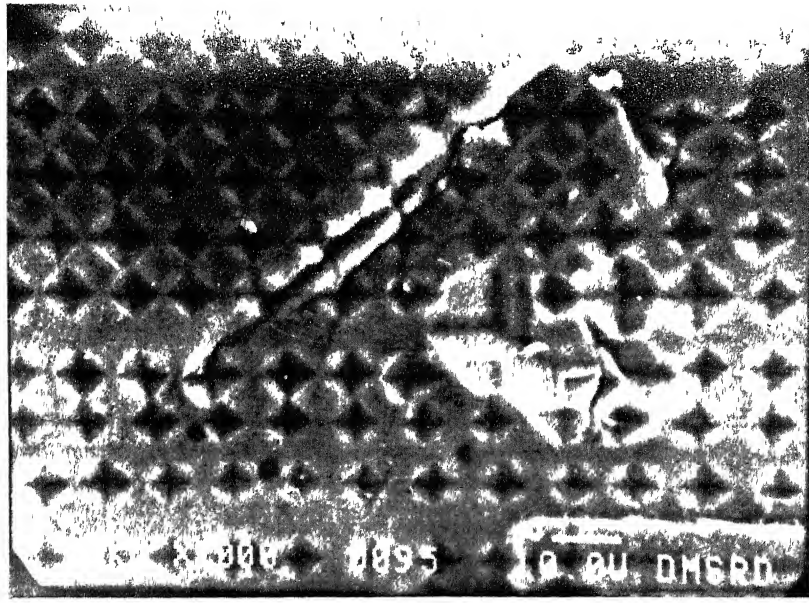
Fig 22 SEM study of fig. 21, but taken at a higher magnification. Conditions are same as in Fig 21.
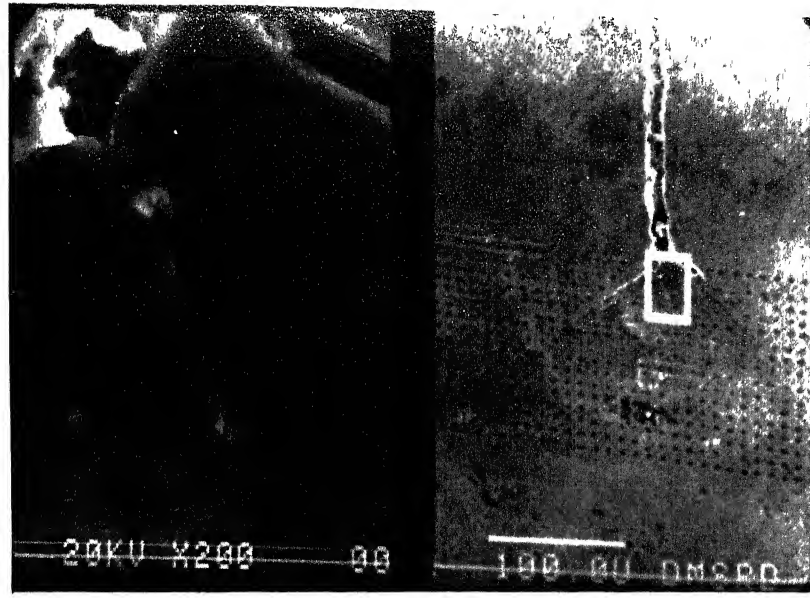
Fig 23 Same conditions as Figs. 21 and 22, but taken at a lower magnification on the R.H S., and a small portion is also shown at a 2000X times higher magnification on the L H S. through SEM photograph. Micro-grid elongation is visible below the root of an yielding crack tip. (Take same data as Fig. 21).
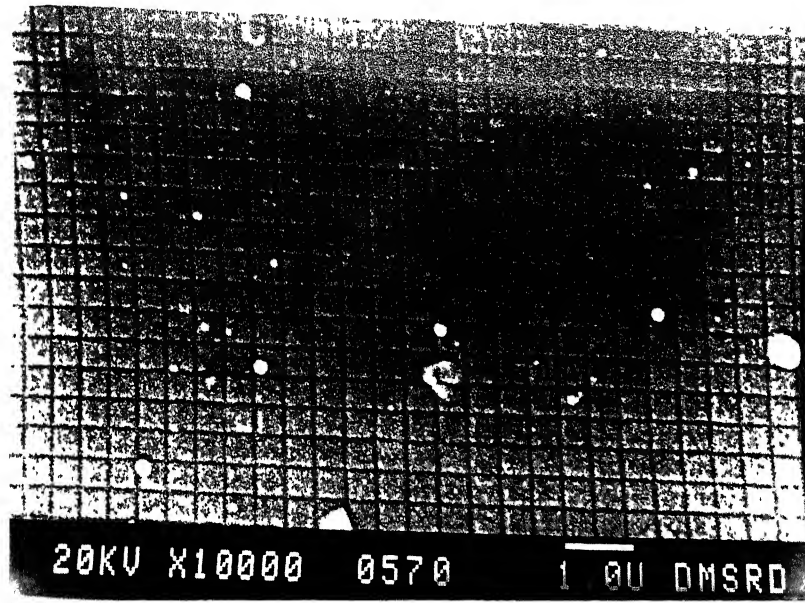
Fig 24 Micro-grid photographs by SEM. Transmission Electron Microscope cross-grid calibration piece from polaron Co, England, is mounted on copper foils. Carbon replica thickness is in the order of 400 A_o. Replica square grid lines shown here, has pitch = 0 47 μ. Line thickness = 0.06 μ, such T.E.M. calculation piece is glued on the surface of a 7075-T6 aluminium specimen near the crack tip region. by silastic (silicon) rubber adhesive, which can take large strain deformation.
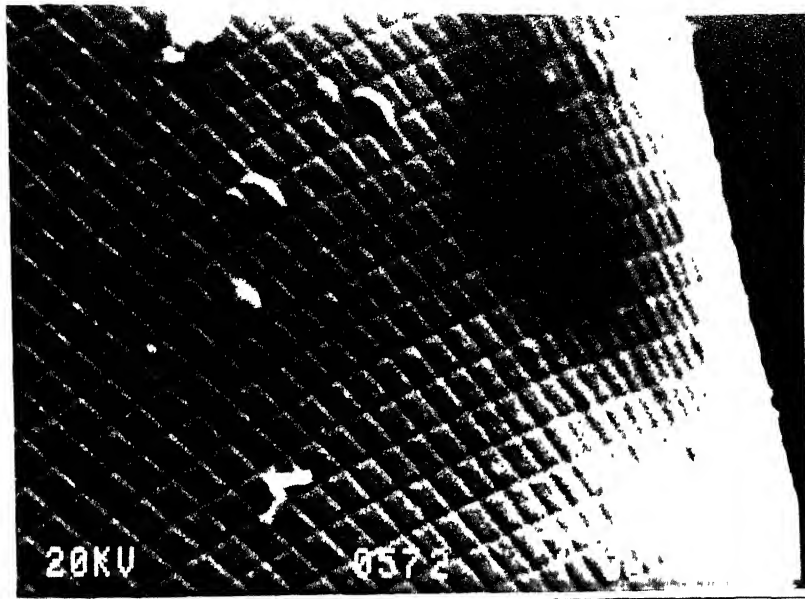
Fig.25 SEM photo for a crack tip micro-grid distortion study. TEM square grid pitch distance = 0.47 μ Radial flow pattern is visible below the crack tip due to metal extrusion Material 7075-T6 aluminium. Crack size = 3.41 mm.Pin-loaded tension specimen. Load applied = 8 34 KN. Fatigue pre-cracking data $\triangle K_I = 9 Mpa \sqrt{m}$ with R = 0 1

Tracing of Fig 25

1.0 μ
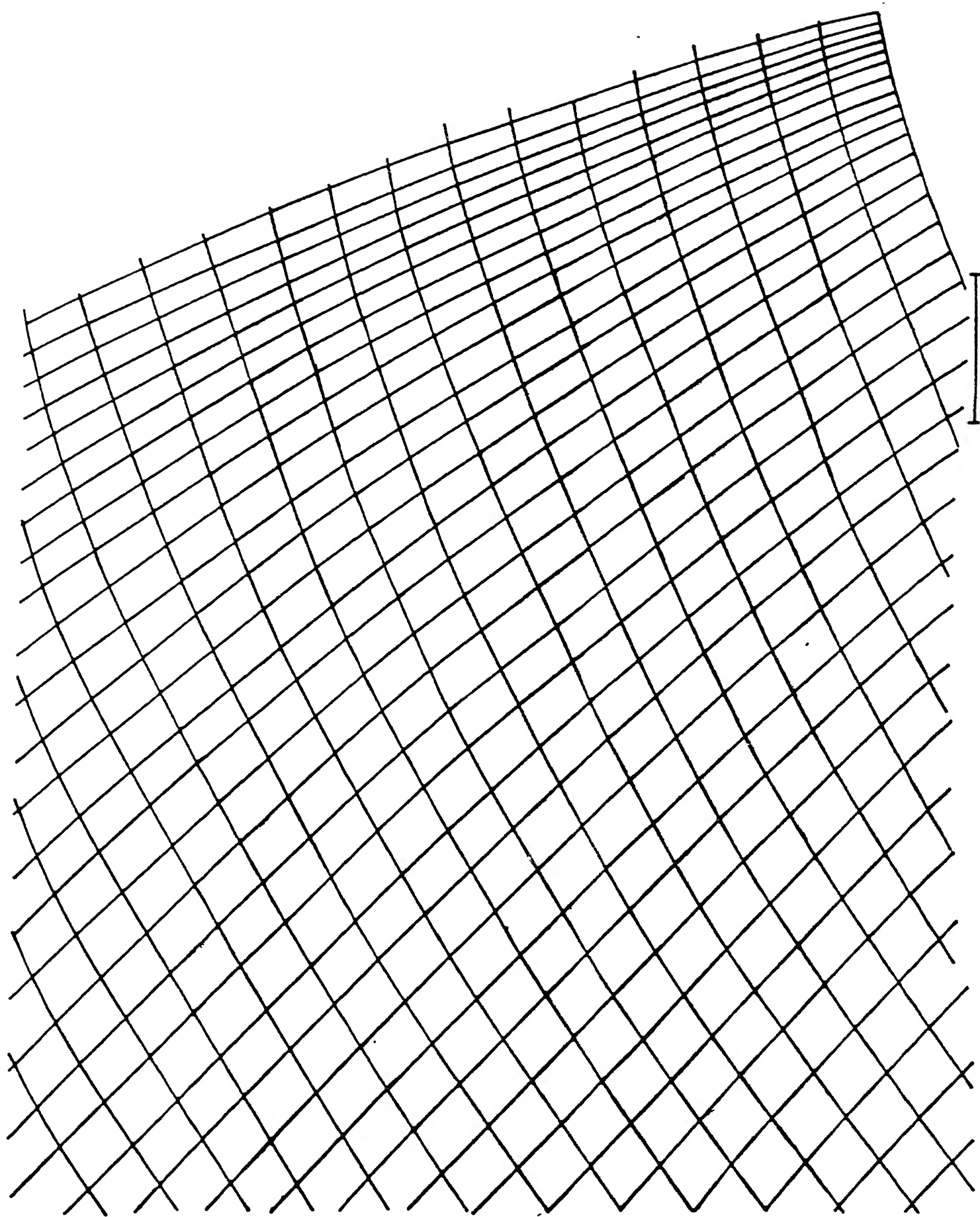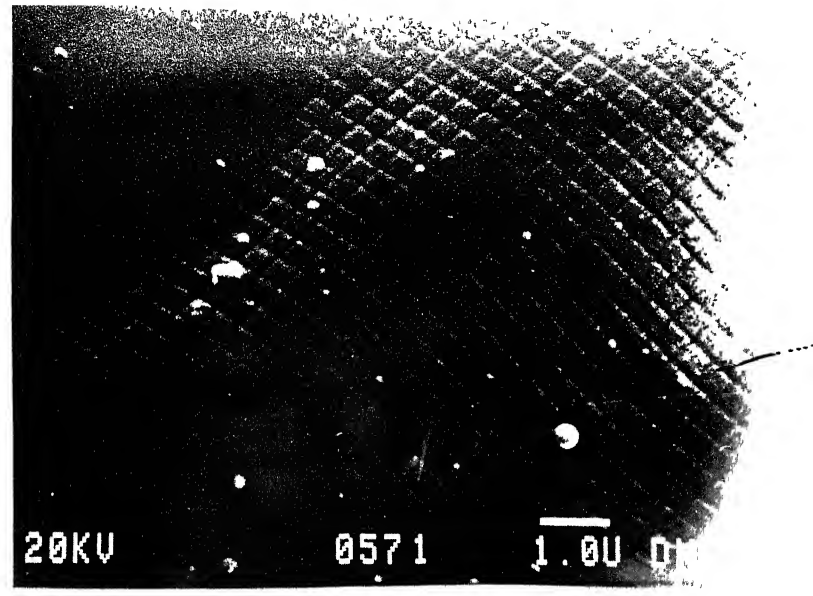
Fig. 26 SEM photograph of a carbon replica micro-grid distortion at a crack tip taken on 45^0 plane with respect to the extension direction Shear strain distribution with in the yielded zone has been measured on the surface of a cracked specimen.Material; 7075-T6 aluminium alloy Crack size = 3 69 mm. Pin-loaded tension specimen. Load applied = 8 34 KN Fatigue pre-cracking data $\triangle K_I = 9Mpa \sqrt{m}$. Original square grid pitch distance = 0.47μ.

1 0 ''

Tracing of Fig. 26

54
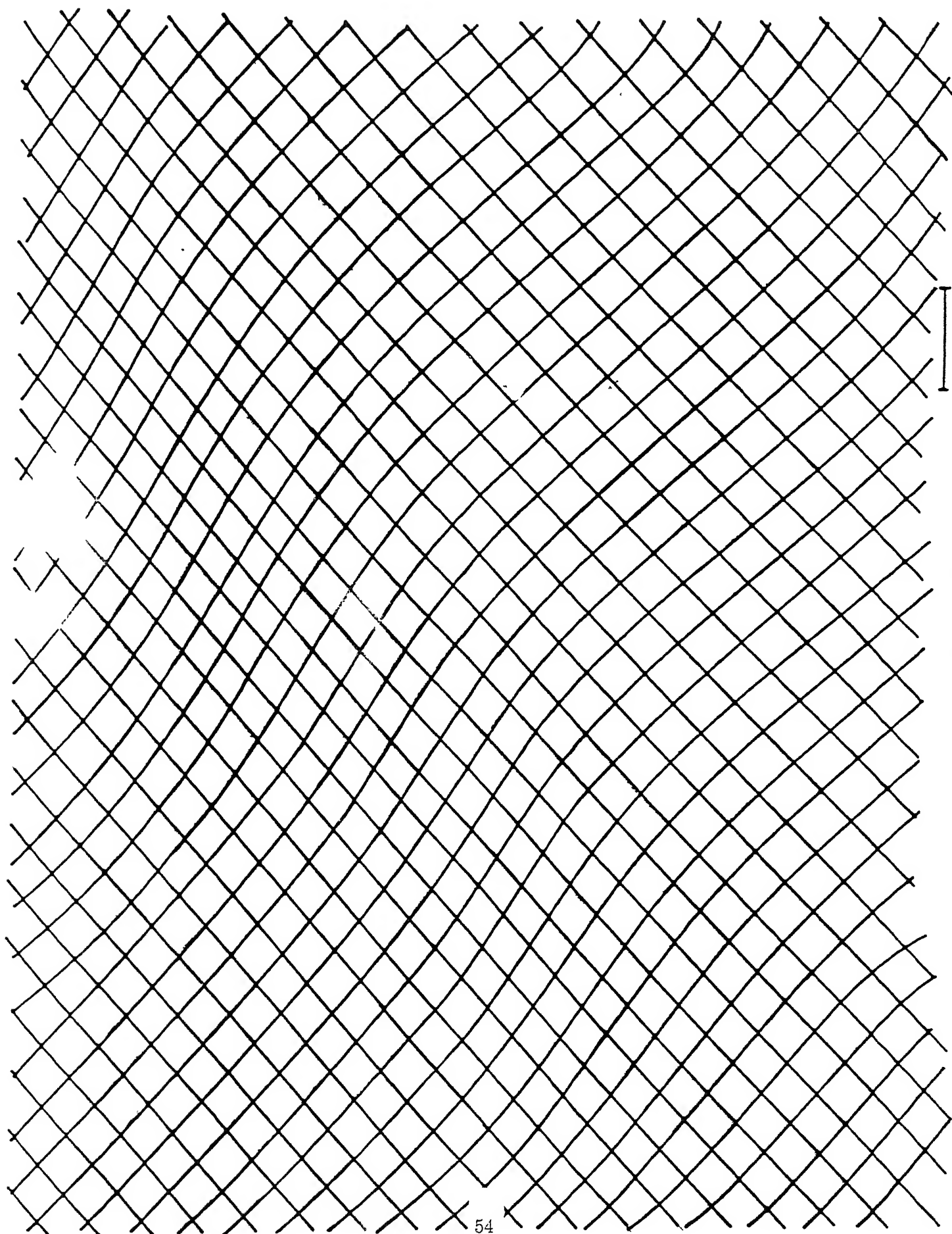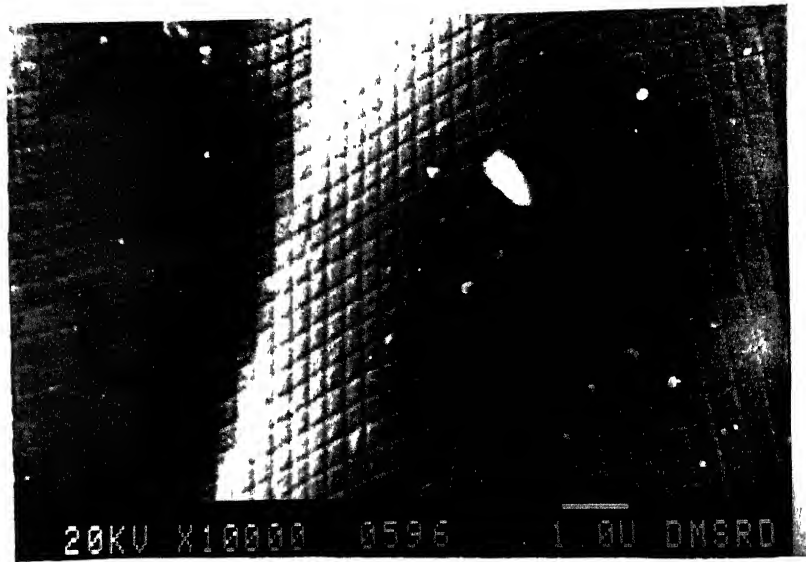
Fig 27 SEM photograph on a crack-tip with TEM calibration carbon replica square grids mounted. Plastic strain distribution is visible ahead of crack tip. Strains have been measured by grid distortion study. Mixed flow field is visible Material; 7075-T6 aluminium alloy. Crack size = 3.41 mm. Pin-loaded tension specimen. Load applied = 11 KN. Fatigue pre-cracking data $\triangle K_I = 9Mpa \sqrt{m}$ Measured original square grid pitch line distance = 0.47 μ , Readings were taken near 45^0 line w.r.t. crack extension plane.

1.0 μ
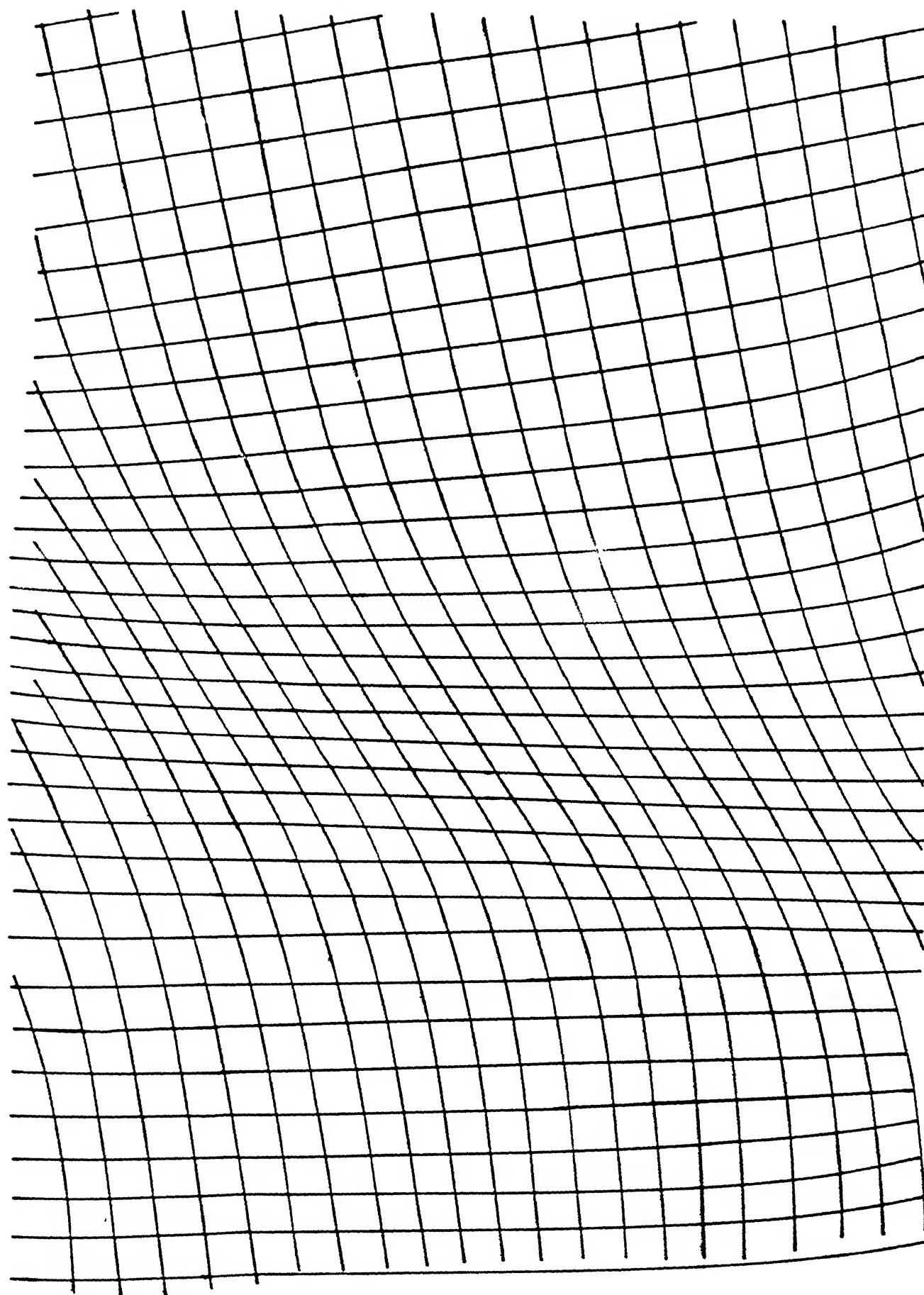
Tracing of Fig 27
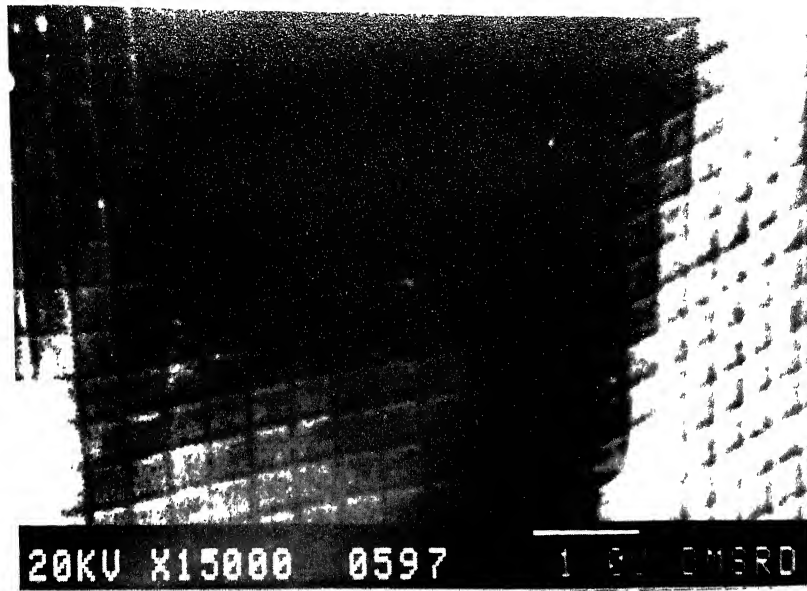
Fig 28 SEM photograph taken at a higher magnification on crack tip plastic flow in 7075-T6 aluminium alloy Strain fields are measured from such photographs taken at various points ahead of a tip. Crack size = 3.41 mm. Pin-loaded tension specimen. Load applied = 11 KN. Fatigue pre-cracking data $\triangle K_I = 9Mpa \sqrt{m}$. Original square grid pitch distance = 0.47 μ. Similar observations were made at various angles at different points with the yielded zone.
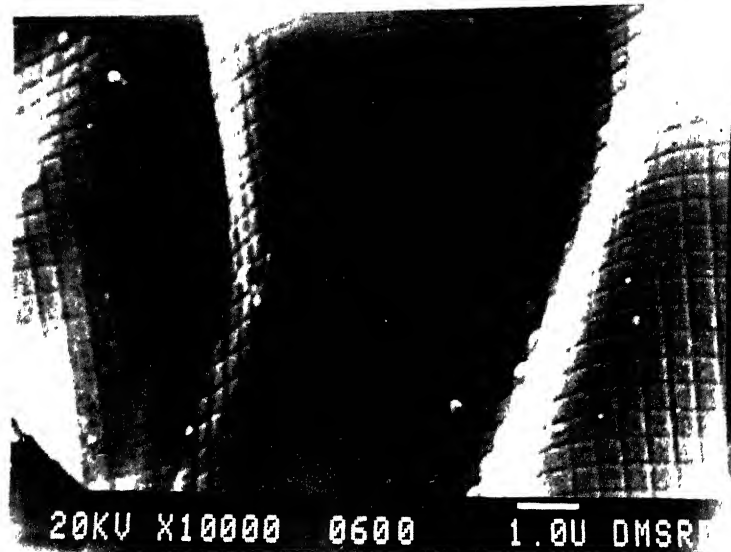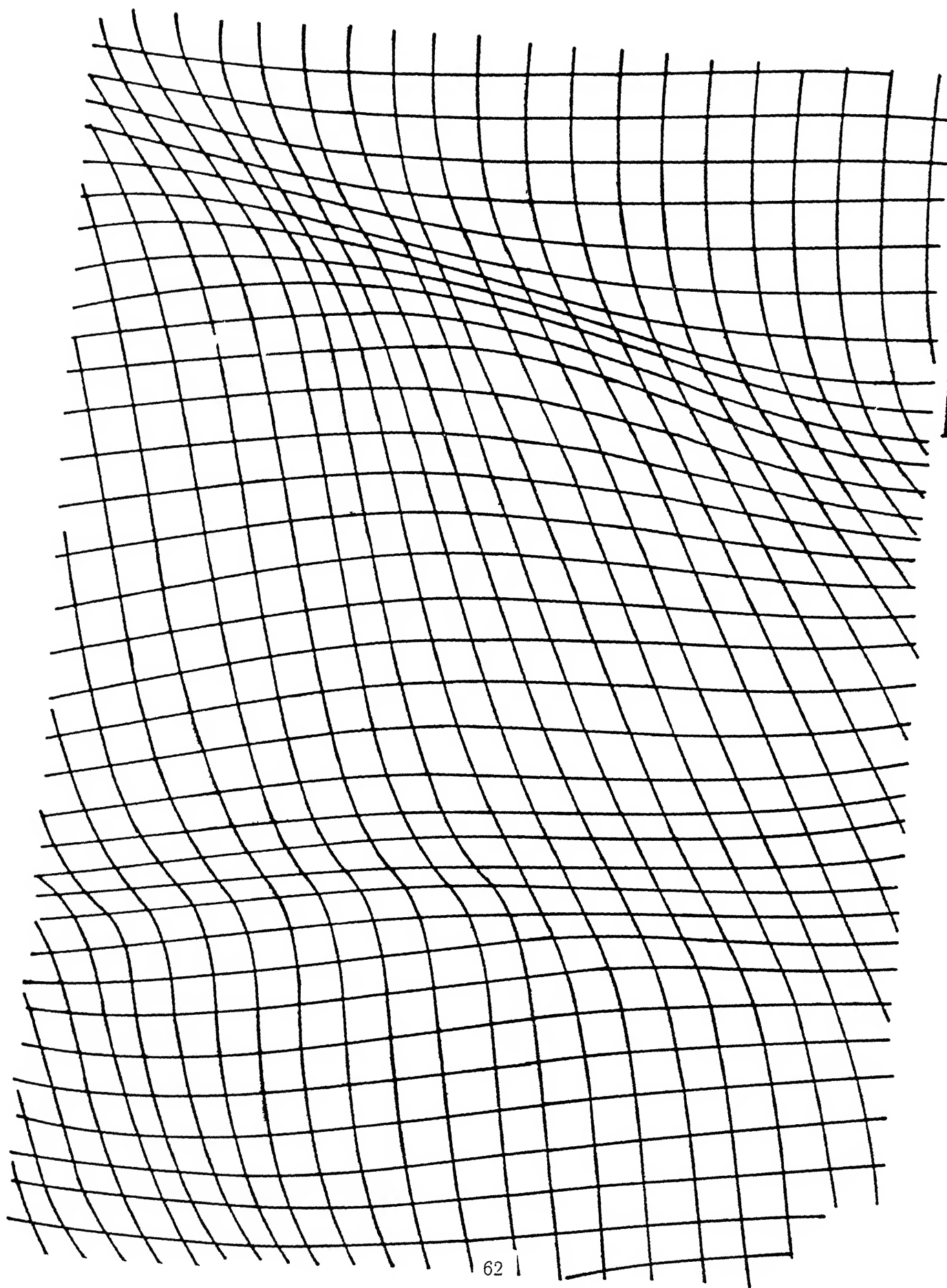
Tracing of Fig 28

1.0 μ
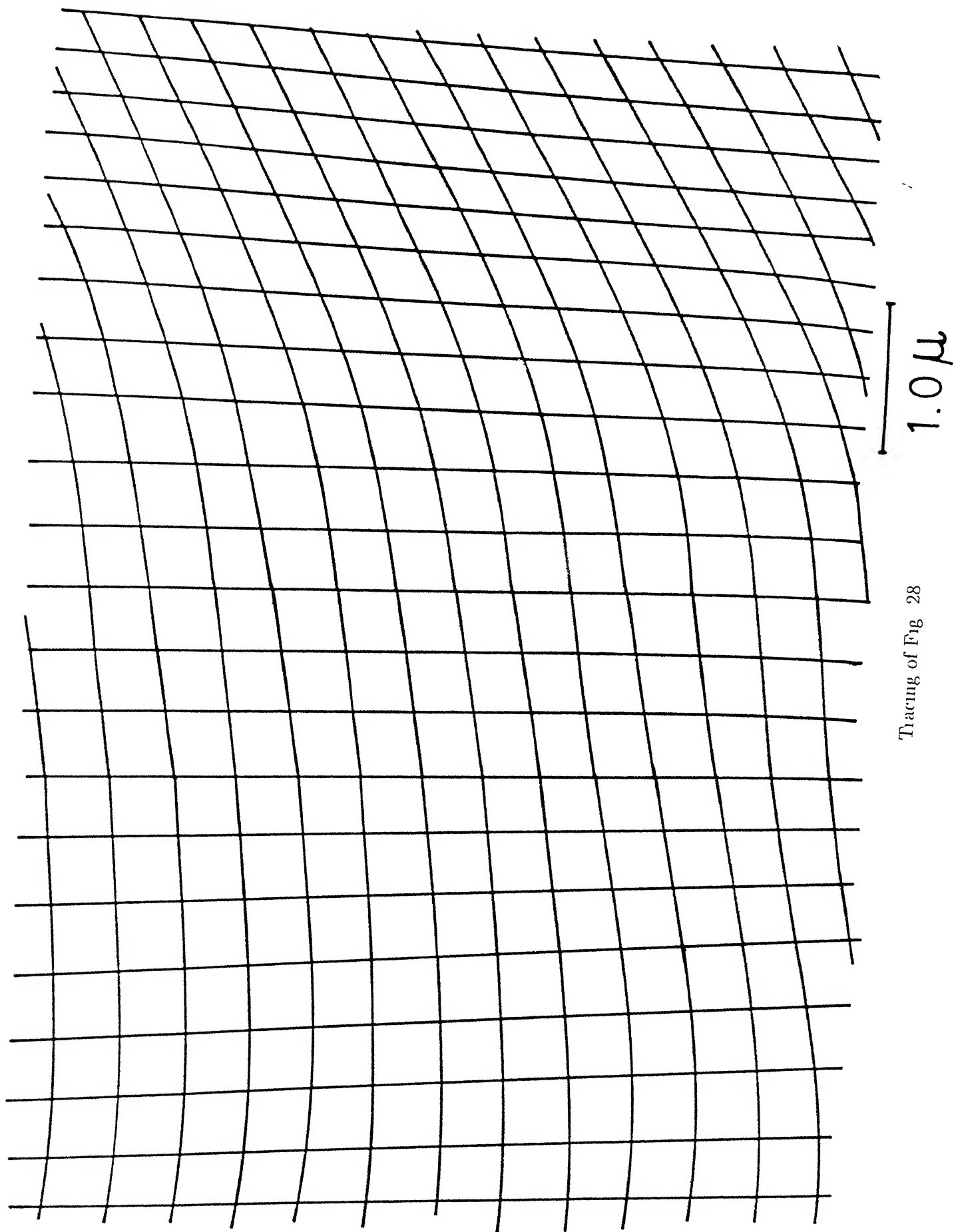
58
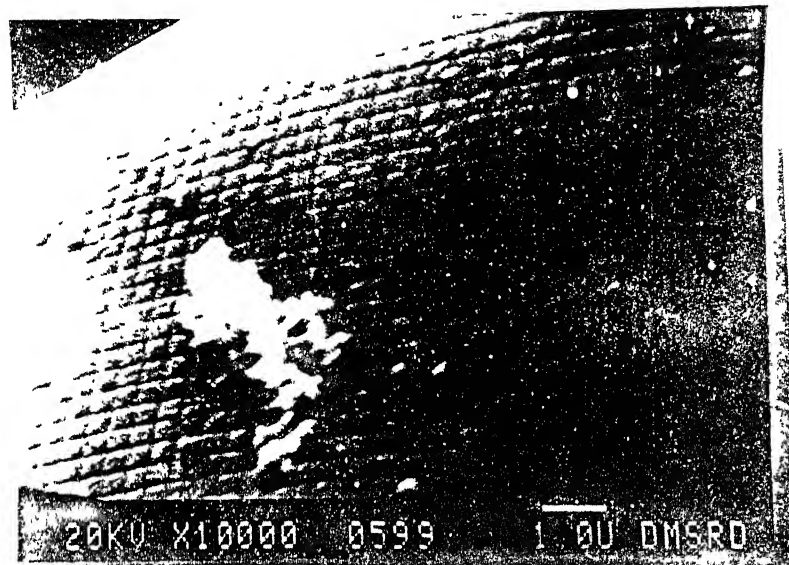
Fig. 29 SEM photograph of carbon replica grids on crack tip. Radial plastic flow is seen again below the crack tip at a higher load. Crack size = 3.41 mm. Pin-loaded tension specimen. Load applied = 11 KN. Fatigue pre-cracking data $\triangle K_I = 9 Mpa \sqrt{m}$. Original square grid pitch distance = 0.47 μ.

1.0 μ

Tracing of Fig. 29

60
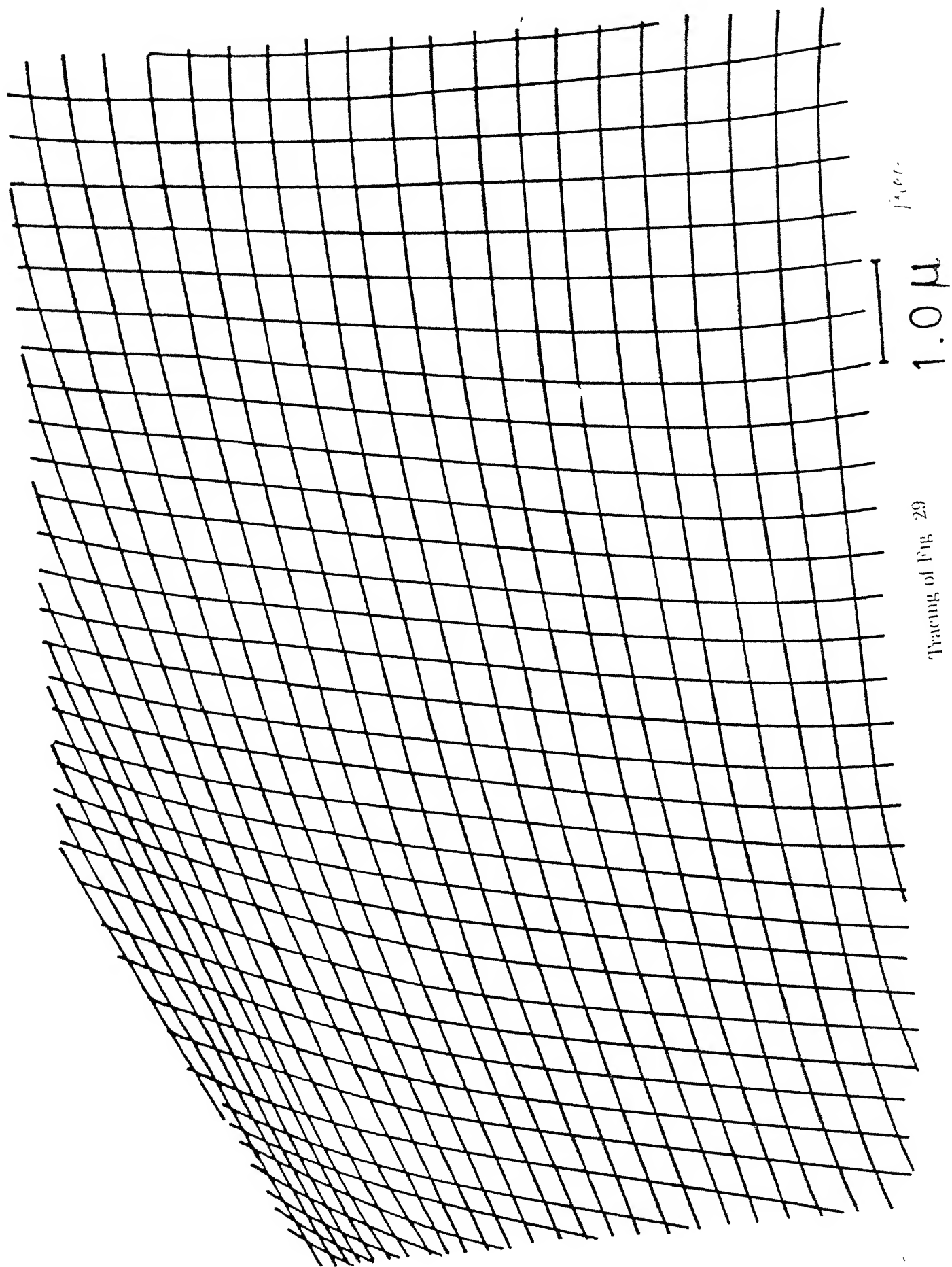
Fig. 30 Strain-localization with shear bands,inside a plastically yielded crack tip. SEM photographs taken on a surface a fatigue cracked 7075-T6 aluminium alloy specimen. Crack size = 3.41 mm. Pin-loaded tension specimen. Load applied = 11 KN. Fatigue pre-cracking data $\triangle K_I = 9 Mpa \sqrt{m}$. Original square grid pitch distance = 0.47 μ. Non homogeneous plastic strain accumulates ahead of the crack tip.Readings were taken on 45^0 plane w.r.t. the crack.
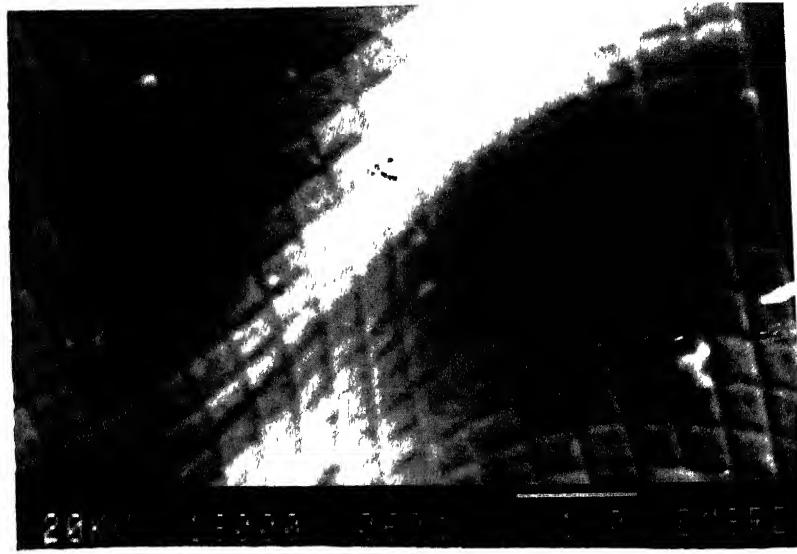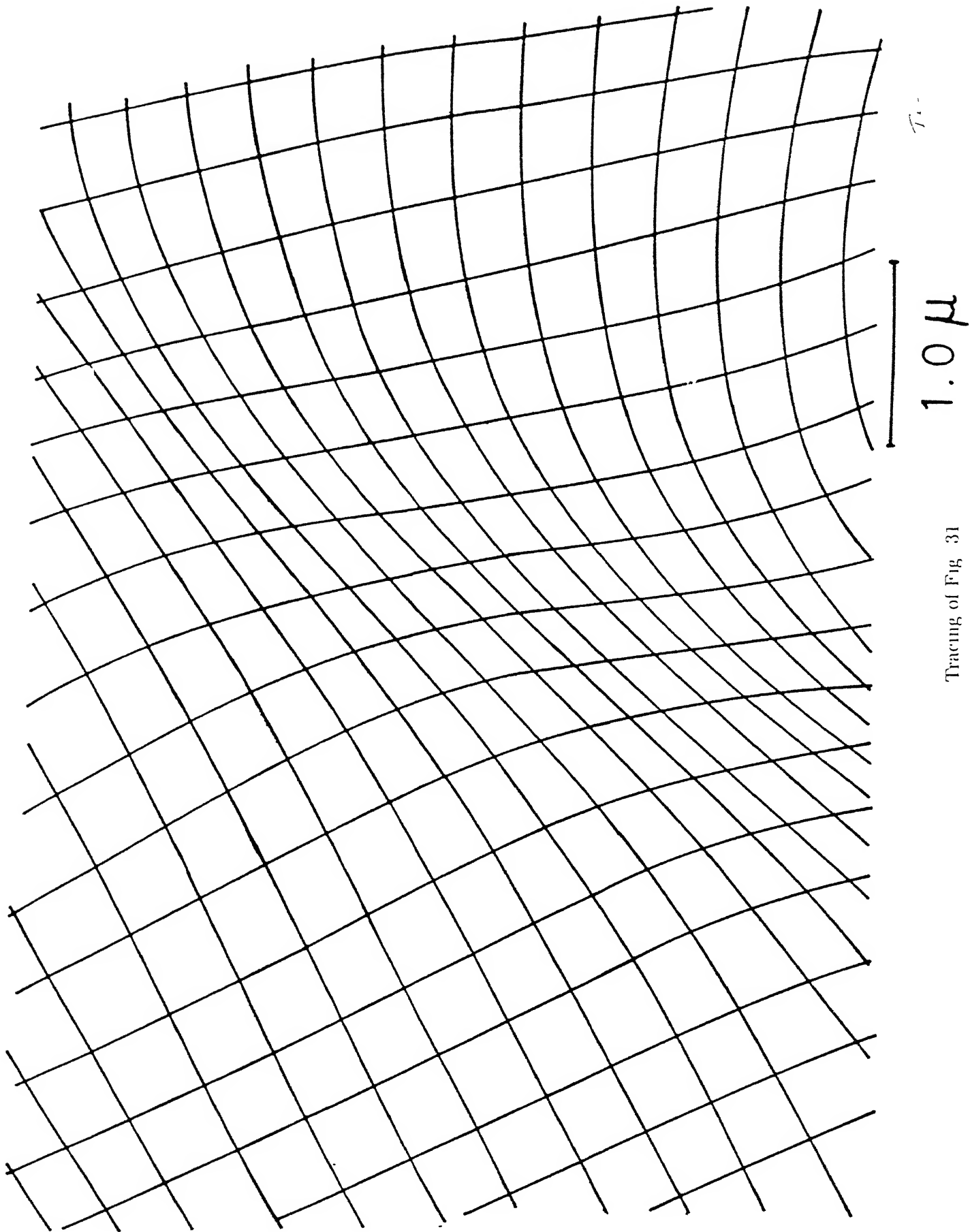
Tracing of Fig 30

1.0 μ

62

Fig 31 Plastic concentration inside the yielded zone at crack tip in 7075-T6 aluminium alloy. Plastic strain distribution is measured by micro- grid distortion method. SEM photograph showing carbon replica grid distortion at crack tip. Readings were taken at various points in different regions on the surface of the specimen. Crack size = 3.41 mm Pin-loaded tension specimen. Load applied = 11 KN. Fatigue pre-cracking data $\triangle K_I = 9Mpa \sqrt{m}$ Original square grid pitch distance = 0.47 μ. Non-homogeneous plastic flow is confirmed from the grid distortion.
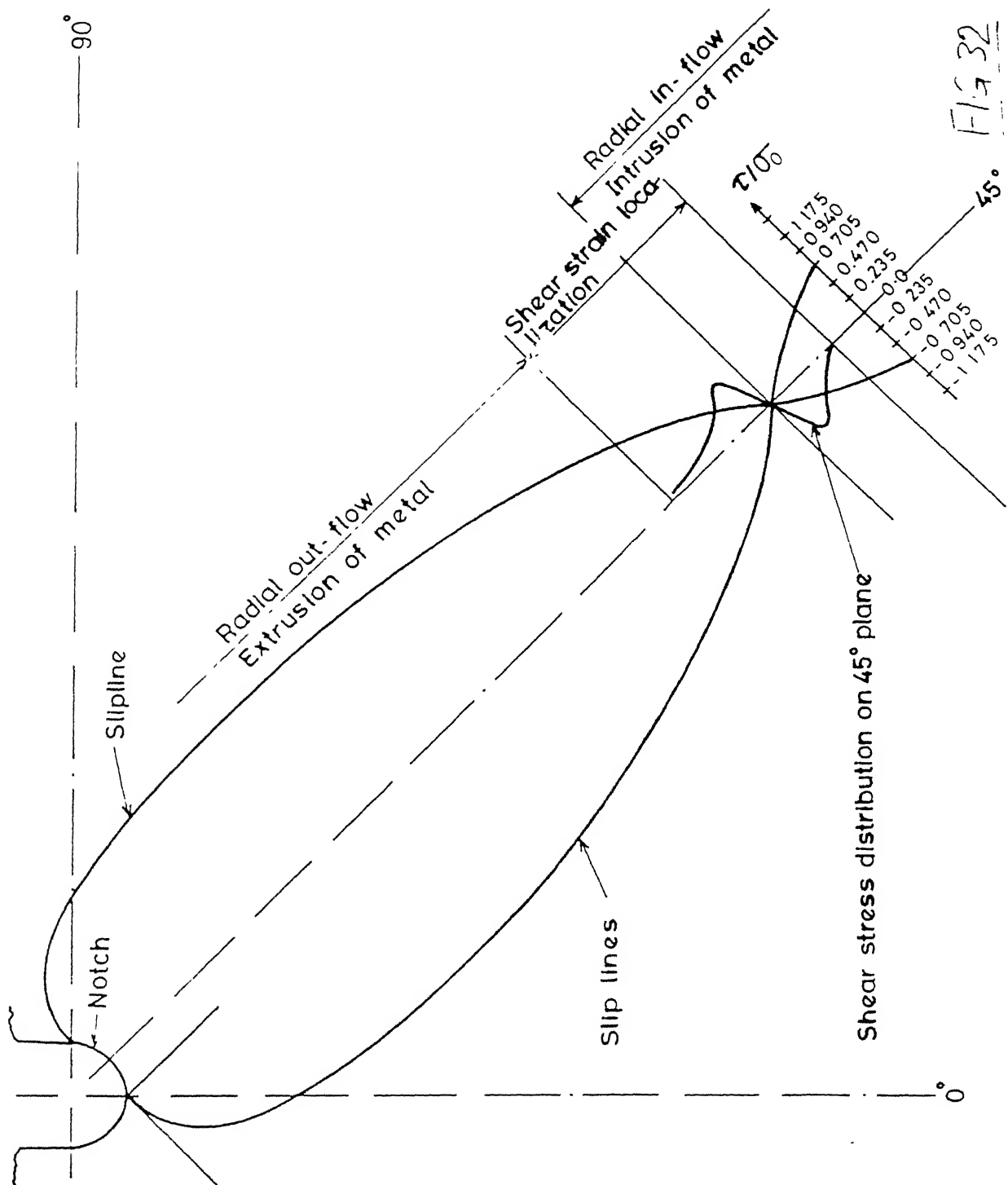
1.0 μ

Tracing of Fig. 31

Fig. 32 Shear stress concentration is plotted on 45° plane with respect to the crack. Stress calculation is based on slip line field theory described in the text. Graphical construction was employed. Slip lines are drawn from experimental observations. Mixed stress field is noticed Shear localization is due to the intrusion-extrusion of metal. Material 7075-T6 aluminium alloy. Test conditions are exactly the same as described in figs. 27 to 31.
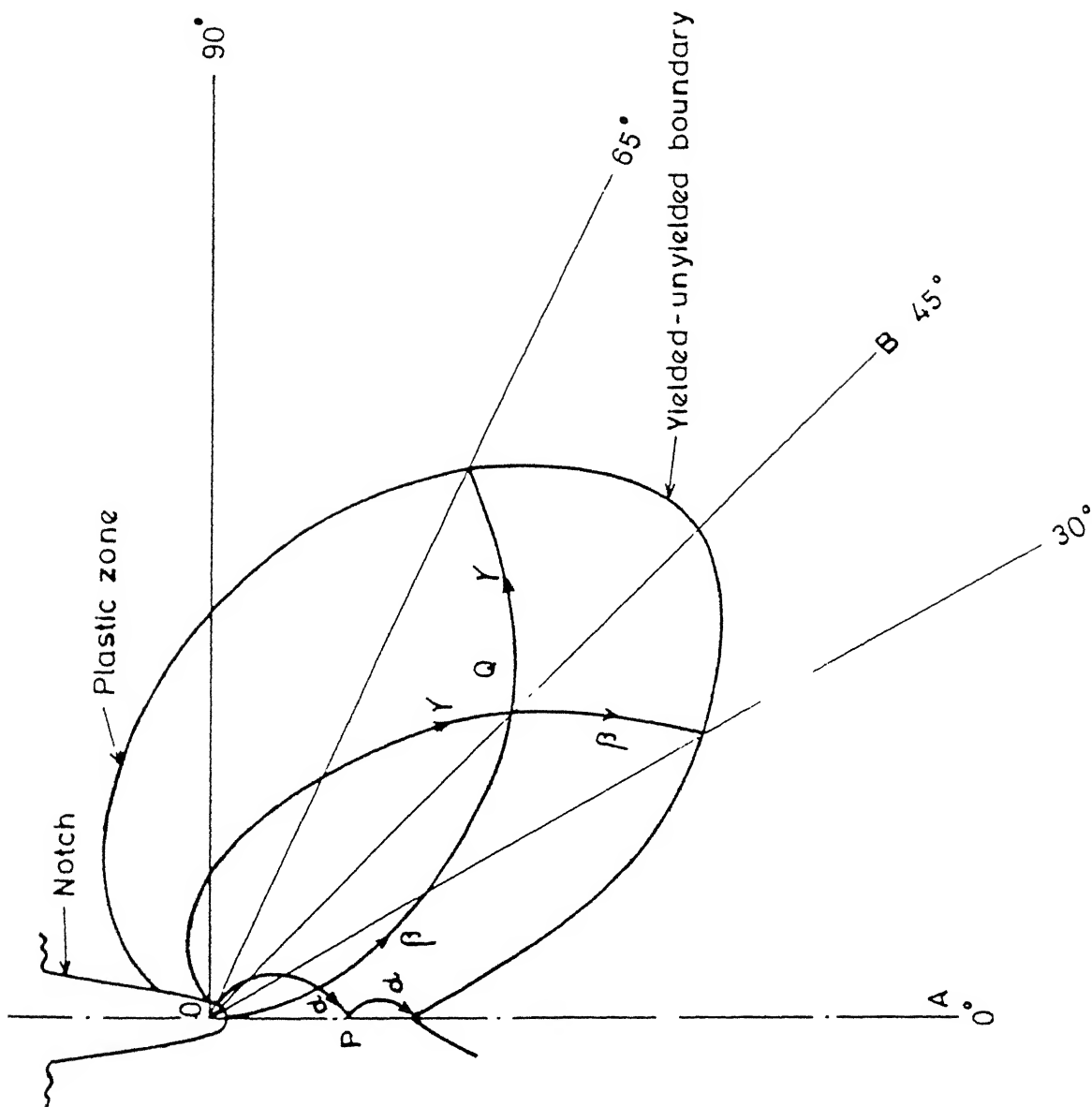
65

Fig 33 Slip lines proposed from the expermental observations on crack tip plastic flow alpha is the well known slip line due pure bending action on the notch about plane OA (i.e. 0^0 plane) γ is another slip line due to the bending action about OB plane. beta slip line has also been observed expermentally while studying the shear deformation ahead of the crack tip. This is based on the study of plastic flow at crack tip in 7075-T6 anisotropic aluminium alloy. Stress concentrations are seen to occur at P and Q. Micro-fracture can take place in these regions.

Chapter 2

WARM PRE-STRESSING EFFECT ON FRACTURE TOUGHNESS OF MILD STEEL

2.1 INTRODUCTION

This part of the thesis deals with the warm pre-stressing effect on crack toughness of mild steel. Firstly, a cracked beam is loaded at room temperature, and then, the beam is fractured at sub-zero temperature. Toughness is seen to increase at this temperature due to warm pre-stressing. The prominent theme of the thesis has been to find the relationship between the brittle fracture and plastic deformation.

If one plots the uniaxial tension as a function of temperature, in ferritic steel, it rises rapidly with falling temperature. The classical theory of fracture of a potentially ductile material fracture in brittle is investigated in this chapter. The entire ductile brittle transition behavior of mild steel is studied from looking into the effect of warm pre-stressing Above the embrittlement temperature cleavage fracture can still occur, if the specimen contains a notch or a crack, sharp enough to give the plastic constraint,superposing a triaxial tension and raising the general tensile stress during plastic yielding. Thus, the warm pre-stressing on notch embrittlement is studied at sub-zero temperature. There-

fore, plastic deformation is an essential part of the brittle fracture of metals. It may nucleate cracks of the critical size required by the Griffith fracture condition, or it may be able to propagate by a mechanism different from that of the Griffith theory. Thus, the strain strengthening is playing on important role in fracture.

Once a crack is found on a cleavage plane, the only work required for brittle fracture is that needed to break the interatomic bonds at the crack ends and this can usually be provided by the elastic energy at the specimen As the crack does not require thermal activation the velocity of crack propagation can be very high, about half the speed of the shear waves in the material. Because of the large amount of work expended in plastic deformation, ductile fracture propagates at much lower velocities, and in certain cases fracture can be stopped. Thus, brittle and ductile fracture can be distinguished by their mode of propagation, even though in both cases the deformation may be of a ductile nature prior to the start of crack propagation. Many solids like mild steel, can exhibit both brittle and ductile fracture characteristics, depending on the mode of stressing, the rate of application of the load, and the temperature.

2.2 RESULTS

Fig. 2.3 shows the effect of fracture toughness on warm pre-stressing. Firstly, a cracked beam in loaded upto 70% of the fracture load at room temperature.Then the sample is broken at sub-zero temperature. Temperature range was from -80^0 C to $+50^0$ C. Ductile-brittle transition behavior is seen to occur, which is plotted in the figure. Next, same thing was repeated at 80% of the fracture load at room temperature. Thus, the sample is loaded in Fig. 2.4 upto $0.8P_c$, when P_c is the fracture load at room temperature(Fig. 2.5 and 2.6). Some samples were tested without warm pre-stressing at room temperature, which is shown in Fig. 2.7. Fig. 2.8 shows the K_{IC} plot against warm pre-stressing effect. From 50% to 60%. there is no change in toughness. However, above 60% warm pre-stressing, there is an increase in toughness.Therefore, due to warm pre-stressing fracture toughness of the metal is increased

2.3 DISCUSSION

At room temperature, when a notched beam is loaded, the plastic deformation spreads at the tip of the crack. The material is permanantly damaged in this region. More volume of material is deformed compared to the same at sub-zero temperature. Bandyopadhyay [30 − 33] model shows the interaction mechanism, between the free notch surface and the radial stress discontinuity. This means, at a larger distance from the crack tip, the material is damaged, and cracks, voids etc appear locally in this region. When the specimen is loaded at room temperature, such damaged material remains there, even if the sample is dipped into a lower temperature. The surface insteability load will be more at lower temperature due to increased interaction stress. Thus, at low temperature, higher crack extension force will be needed to extend the crack. Fig. 2.3 to Fig. 2.6 show continuous increase of toughness with temperature. Ductile-brittle transition behaviour is seen to occur in all the cases. Fig 2.8 shows the increase in crack-toughness due to warm pre-stressing effect.
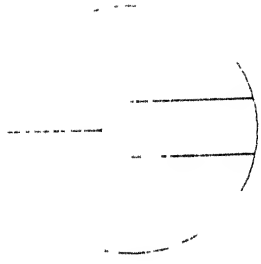
L= W= 8 mm
W= 12mm
B= 12mm
a Varies from 4 to 8mm
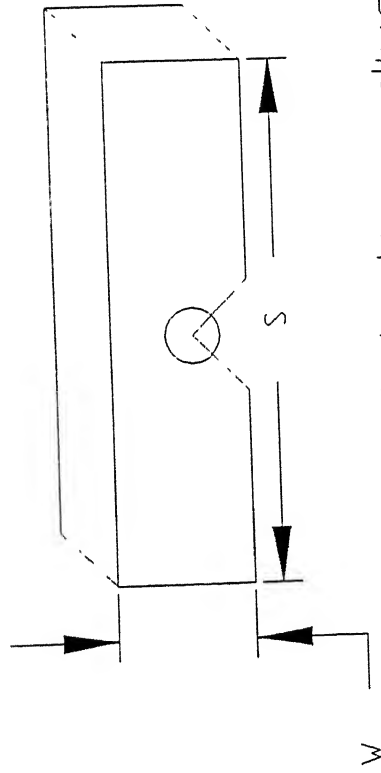
Notch tip radius=R

(a) Notch tip radius=R
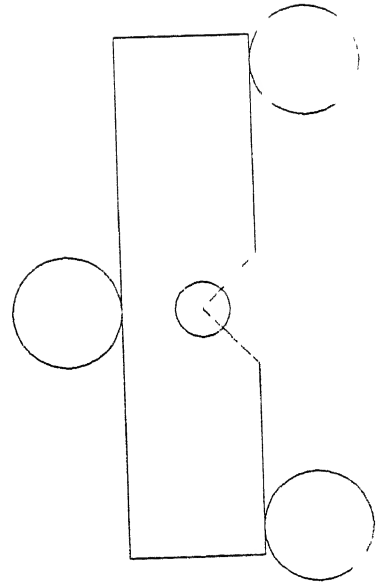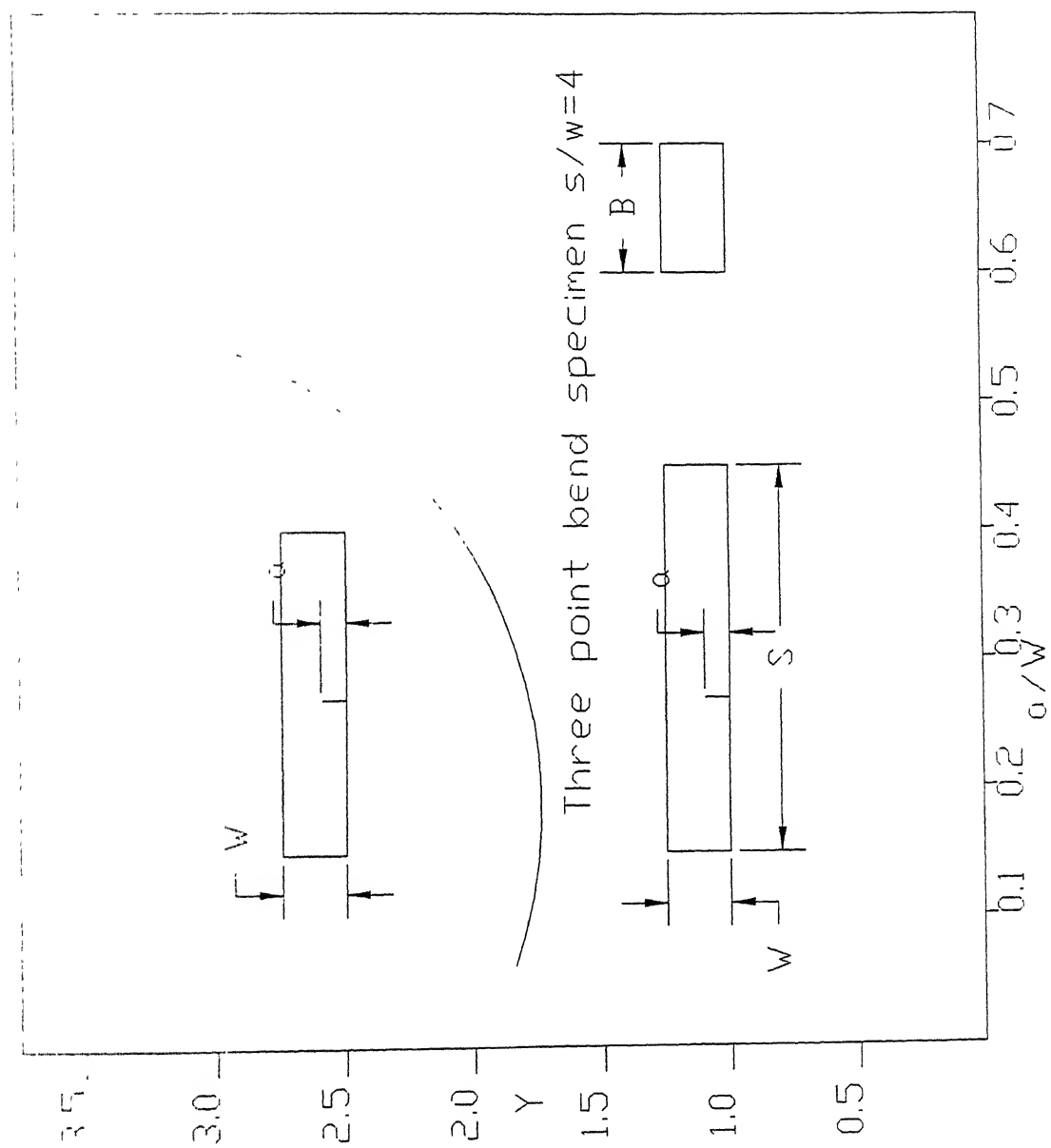
(b) Threepoint bending

Fig 2.6 Fracture test specimen
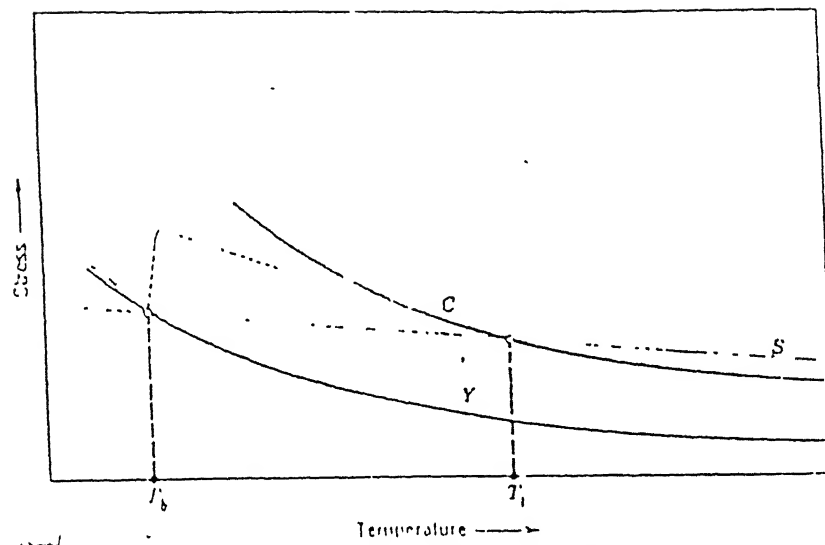
Fig 2P Factor for three point bend specimen

Fig 2 2 Y is the uniaxial and C is the notch-constraint yield stress, S is the fracture stress for cleavage fracture The dashed curve parallel to, and just above, Y is the curve of cleavage-fracture stress in uniaxial tension below T_b The dotted curve shows the locus of ductile fracture of notch specimens above T_b
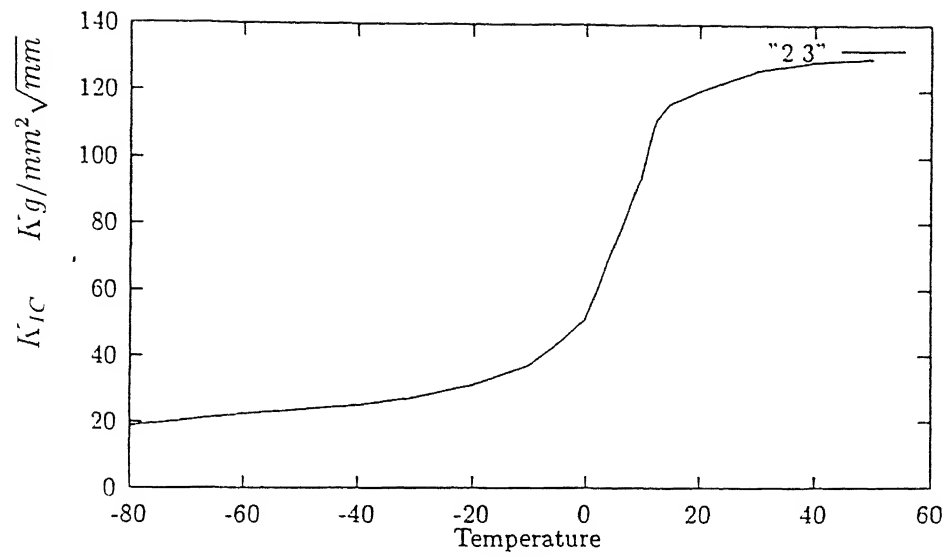
Fig 2 3 Fracture toughness tests at different temperatures when warm pre-stressed at 70% of the Crack extension load

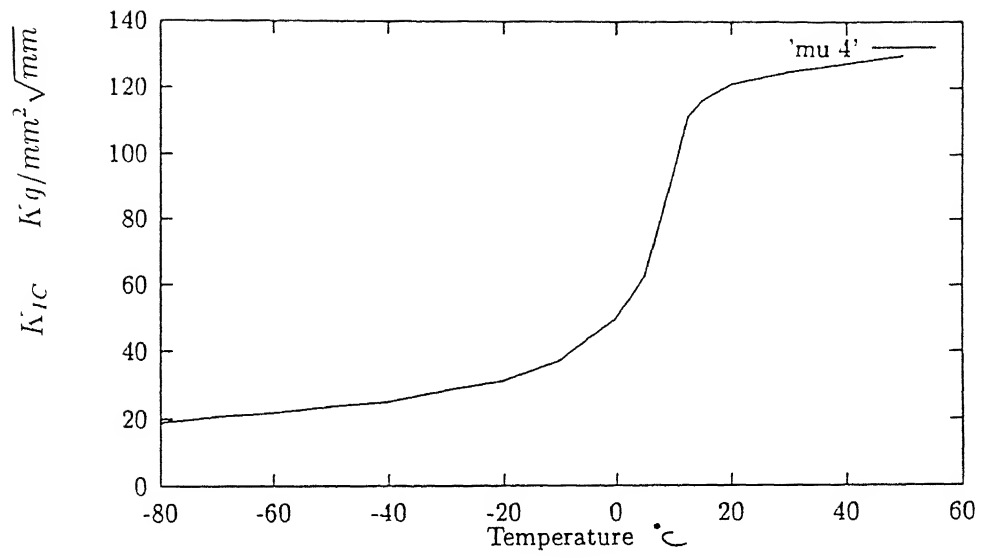Fig 2 4 Fracture toughness tests at different temperatures when warm pre-stressed at 80% of the Crack extension load"
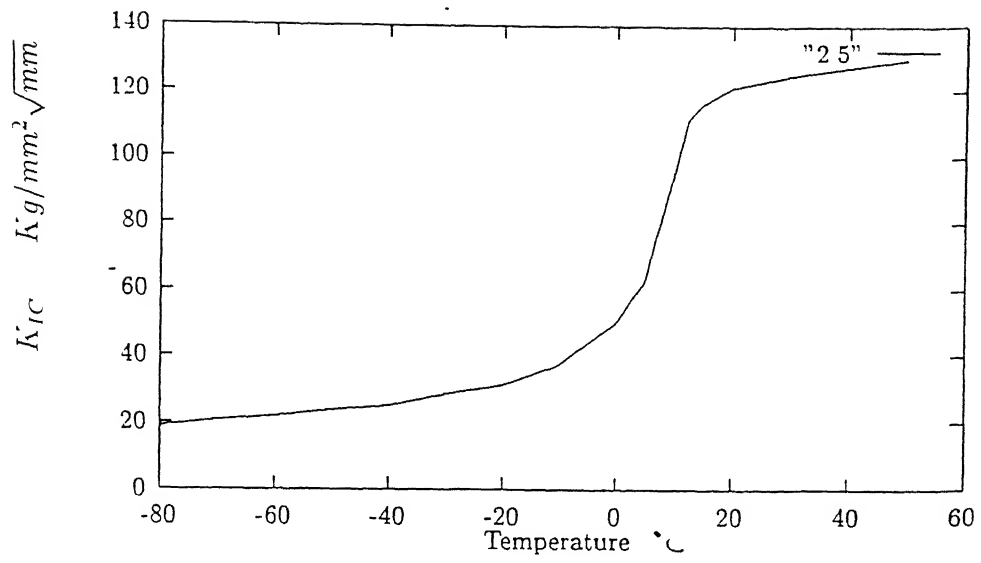
Fig 2 5 Fracture toughness tests at different temperatures when warm prestressed at 90% of the Crack extension load
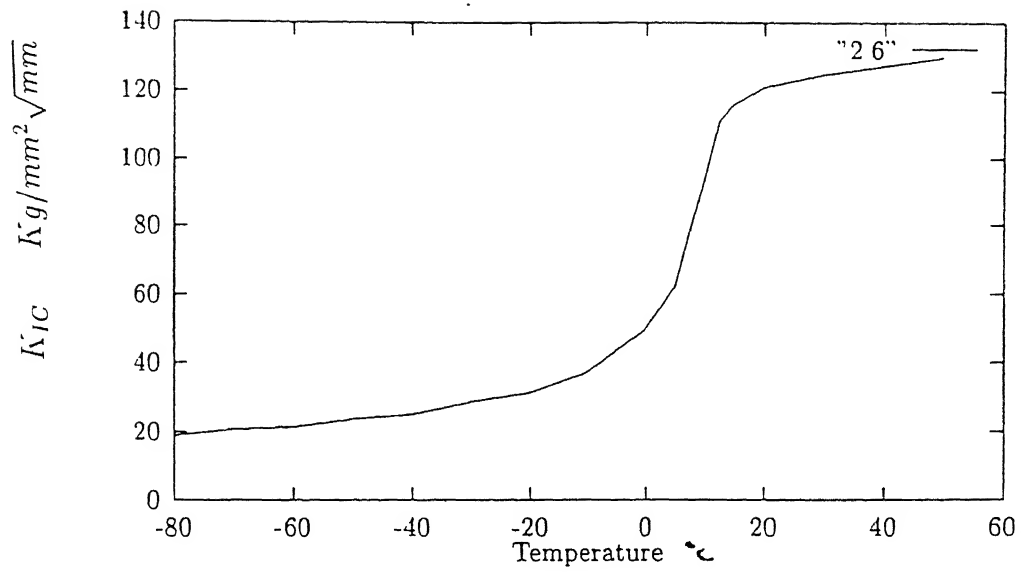
Fig 2 6 Fracture toughness tests at different temperatures when warm pre-stressed at 95% of the Crack extension load
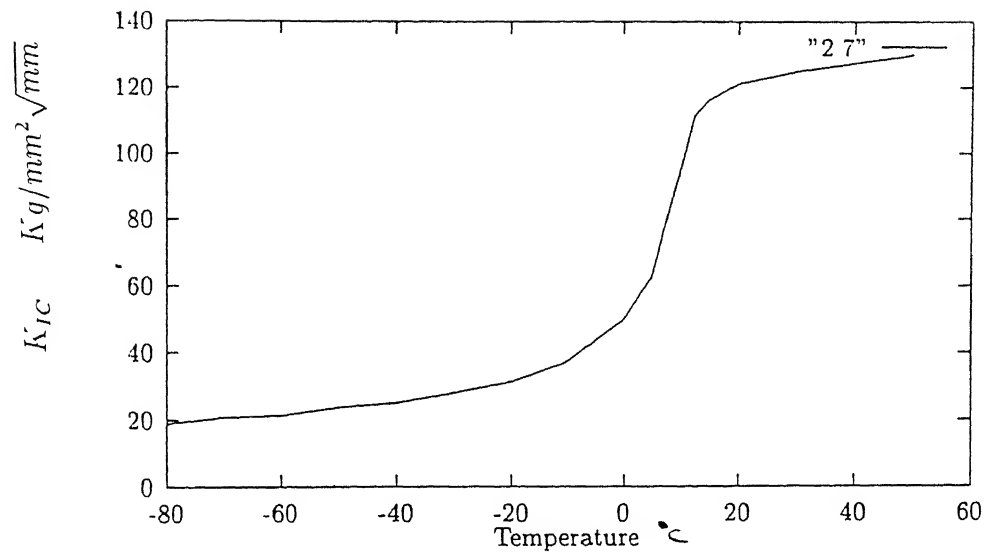
Fig 2 7 Fracture toughness tests at different temperatures when no warm pre-stressing was applied
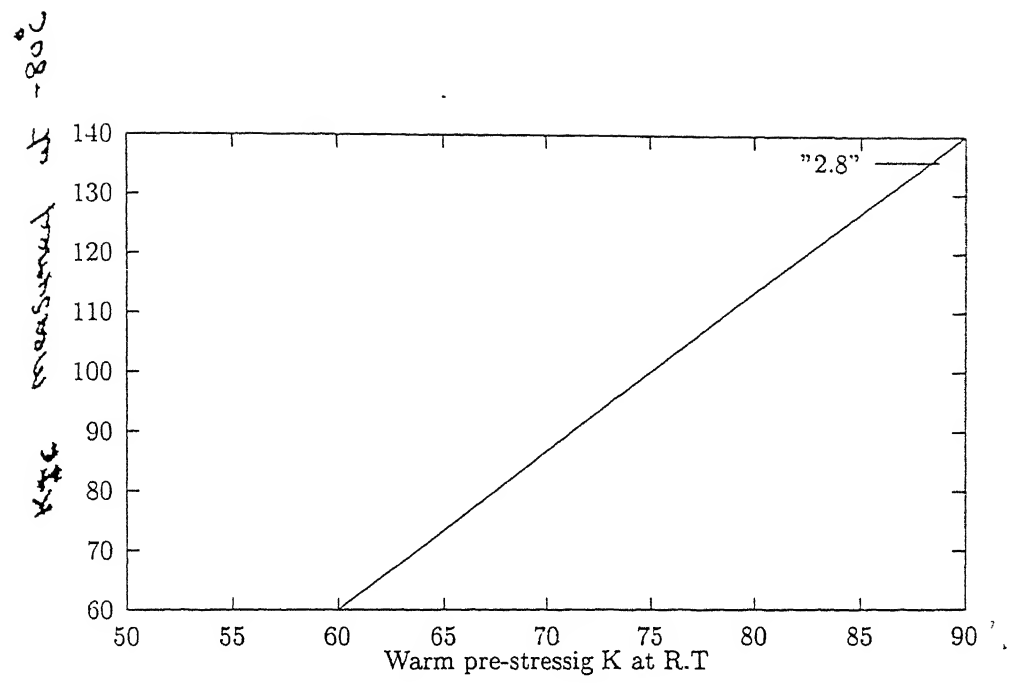
Fig 2 8 Increase in Fracture toughness values against different percentage of warm pre-stressing.

CONCLUSIONS

- Elasticity theory alone is inadequate to describe stable crack extension in elastic-plastic metals.

- Shear strain localization within the plastic enclave is seen to occur before the onset of abrupt crack extension.

- A critical shear stress concentration is needed to extend the crack in a metal

- Part-through semi elliptic crack is seen to form in a circular wire while the crack propagation in helical path.

- Calculations based on Irwin-Sih-Smith overestimates the direction of maximum shear stress vector by 3.3^0 with respect to the axis of the wire.

- Crack toughness increases at sub-zero temperature due to warm pre-stressing.

REFERENCES

1 I Verpoest, B.D. Notohardjono and E. Aernoudt, Fatigue of steel wire and combined tensile and shear loading conditions, International Conference on FATIGUE. held at the University of Birmingham, England, September 1984 (ed. by C.J. Beevers).

2. I Verpoest, E. Aernoudt, A Deruyttere, M Neirinck and U D. Haene, A quantitative assessment of the influence of surface condition on the fatigue limit of drawn steel wires, Conference proceedings, (held in France) (through private communication)

3 I Verpoest, E Aernoudt, A. Deruyttere, M. Neirynck and U.D. Haene, Modeling surface defects as cracks: a new approach to the fatigue limit of steel wires, ICF6, Sixth International Conference on Fracture, held at New Delhi, India, December 1984, Vol. 3, p. 1154.

4 I. Verpoest, E. Aernoudt, et al, Fatigue of engineering Materials and structures, Vol. 3, p. 203 (1981).

5. I. Verpoest, The fatigue threshold, the surface condition and the fatigue limit etc Ph.D. thesis, 1982, Katholieke Universiteit, Belgium.

6. K. Mols, Invloed van de Anisotropie op de Veroe iingscheurgroei bij staaldraad. Ph.D. thesis, 1987, Katholieke Universiteit, Belgium.

7 G.R. Irwin, Crack extension force for a part-through crack in a plate, J. of Applied Mechanics, Trans. of ASME, p. 651, December 1962.

8. G.C. Sih, Experimental Fracture Mechanics, Strain Energy Density Criterion, Mechanics of Fracture, (ed. by G.c. Sih), Vol. 7, Introductory Chapter. Martinus Nijkoft publishers (1981).

9. C.W Smith, Observation on sub-critical flaw growth in complex body geometries, proceedings of the symposium on Absorbed specific Energy/Strain Energy Density Conference, held at Budapest, Hungary, Sept. 1980. p. 271, (ed. by G.C. Sih, E. Czoboloy and F Gillemot), Sijthoft and Noordhoft, Alphen aan der Rijn (1981).

10. B I.G Barr, W T. Barr, W.T. Evans, J. Watkins and B.B. Sabir, Predictions of crack path by photoelasticity and the finite element method, proceedings of the symposium on Absorbed Specific Energy/Strain Energy Density Conference, held at Budapest, Hungary, Sept. 1980, p. 255, (ed. by Noordhoft, Alphenmaan den Rijn (1981).

11. L.S. Sreenath, K.S.S. Aradhya and K. Ramesh, Applications of transmitted-Light etc . ., Sixth International Conferer ence on Fracture, held at New Delhi, India, December 1984, p. 83.

12. J C. Newman Jr. and I.S. Raju, Stress Intensity factors for Internal Surface Cracks in Cylindrical Pressure Vessels, J. of Pressure Vessel Technology, November 1980. Trans. of ASME, Vol. 102, p. 342.

13. C.W. Smith, W.H. Peters, G.C. Kirby and A. Andonian, Stress intensity distributions for natural flaw shapes etc., Fracture mechanics, 13th Conference, ASTM. STP 743, p.- 422 (1981).

14. R.A. Verbraak, private communication with professor and Head of Materials Science, Afdeling der Werktulgbonwkunde, Technische Hogeschool Twente, Enschede, Holland.

15. J. Eftis and N. Subramanion, The inclined crack under biaxial load, Engineering Fracture Mechanics, Vol. 10, pp. 43, 1978.

16. G.C. Sih, A special theory of crack propagation- Intro ductory chapter, Mechanics of Fracture, Vol. I, Methods of analysis and solutions of Crack Problems, (ed. by G.C. Sih), Noordhoff International publishing, Leyden, Holland (1973)

17. R. Muki, Asymmetric problems of the theory of elasticity for a semi- infinite solid and a thick plate, Progress in Solid Mechanics, Vol. I, Chapter III, p.399, (ed. by I N. Sneden and R. Hill), North Holland publishing Company, Holland (1960).

18. I.N Sneden, Fourier Transforms, McGraw Hill, N.Y. (1951). E.C. Titchmarsh, Introduction to the theory of Fourier Integrals, Oxford, 1937.

19. D L. George, Numerical values of some integrals involving Bessel functions, proceedings, Edinburgh Mathematical Society II, Vol. 13, p. 87 (1962).

20. P L B. Oxley, S.W Conning and L.E. Farmer, Investigation of experimental flow patterns for plane strain extrusion of hardening materials with slip line methods, Philosophical Transactions of the Royal Societies (London), Ser. A, Vol. 311, p. 495 (1984).

21. J R Rice, plane strain slip line theory for anisotropic rigid (plastic materials), Journal of Mechanics and Physics of Solids, Vol. 21, pp. 63 (1973).

22. N.K. Chitkara and I.F. Collins, A graphical technique for constructing anisotropic slip line fields, Int. Journal of Mechanical Science, Vol. 16, p. 241 (1974).

23. W. Johnson, M.C. de Malherbe and R. Venter, Some slip line field results for the plane strain extrusion of anisotropic materials through frictionless wedge-shaped dies, Inter national Journal of Mechanical Science, Vol. 15, p. 109 (1973).

24 R. Hill, The Mathematical Theory of Plasticity, Oxford, Clarendon Press (1971).

25. J.F Knott and A.H. Cottrell, Journal of Iron and Steel Institute, Vol. 201, p. 249 (1963).

26. A.P. Green and B.B. Hundy, Journal of Mechanics and Physics of Solids, Vol. 4, p. 128 (1956)

27. W. Johnson, R. Sowarby and R.D. Ventor, Plane Strain Slip Line Fields for Metal Deformation processes, Pergamon Press (1982).

28. G.C. Sih, The mechanics aspects of ductile fracture, Fourth International Conference on Fracture, held at the University of Waterloo, Canada, Fracture ICF4, Vol. 4. p. 361 (1877), University of Waterloo Press.

29. S.N. Bandyopadhyay et al, Stress concentration ahead of an yielding crack tip in brittle aluminium 7075-T651, Report No. GR-2983, Vakgroep Technische Mechanika, Techni sche Hogeschool Twente, Enschede, Twente, Holland (1985).

30. S.N. Bandyopadhyay, Orowan mechanism for abrupt localized flow and fracture initiation in metals ahead of an yielding notch, Engineering Fracture Mechanics, Vol. 16, p. 889 (1982).

31. S.N. Bandyopadhyay, A note on Orowan mechanism below the root of an yielding crack like notch in a strain hardening metal, Engineering Fracture Mechanics, Vol. 16, No. 6, p. 889 (1982).

32. S.N. Bandyopadhyay and V.P. Sharma, Strain localization below the root of an yielding notch, Engineering Fracture Mechanics Journal, Vol. 19, p. 605 (1984).

33. A.S. argon and E. Orowan, Crack nucleation in Mgo single crystals. philosophical Magazine, Vol. 9, p. 1003 and p. 1023 (1964)